

Vortex merging and splitting events in viscoelastic Taylor–Couette flow

Jose M. Lopez[†]

Physics Department, Universitat Politècnica de Catalunya, Campus Nord UPC, 08034 Barcelona, Spain

(Received 21 December 2021; revised 2 July 2022; accepted 2 July 2022)

Recent experiments have reported a novel transition to elasto-inertial turbulence in the Taylor–Couette flow of a dilute polymer solution. Unlike previously reported transitions, this newly discovered scenario, dubbed vortex merging and splitting (VMS) transition, occurs in the centrifugally unstable regime and the mechanisms underlying it are two-dimensional: the flow becomes chaotic due to the proliferation of events where axisymmetric vortex pairs may be either created (vortex splitting) or annihilated (vortex merging). In this paper, we present direct numerical simulations, using the finitely extensible nonlinear elastic–Peterlin (FENE-P) constitutive equation to model the polymer dynamics, which reproduce the experimental observations with great accuracy and elucidate the reasons for the onset of this surprising dynamics. Starting from the Newtonian limit and increasing progressively the fluid’s elasticity, we demonstrate that the VMS dynamics is not associated with the well-known Taylor vortices, but with a steady pattern of elastically induced axisymmetric vortex pairs known as diwhirls. The amount of angular momentum carried by these elastic vortices becomes increasingly small as the fluid’s elasticity increases and it eventually reaches a marginal level. When this occurs, the diwhirls become dynamically disconnected from the rest of the system and move independently from each other in the axial direction. It is shown that vortex merging and splitting events, along with local transient chaotic dynamics, result from the interactions among diwhirls, and that this complex spatio-temporal dynamics persists even at elasticity levels twice as large as those investigated experimentally.

Key words: Taylor–Couette flow, transition to turbulence, viscoelasticity

1. Introduction

The Taylor–Couette flow (TCF) i.e. the fluid flow contained in the annular gap between two vertical concentric cylinders, is a prototypical system to investigate hydrodynamic instabilities and turbulence in rotating flows. If the working fluid is Newtonian and only

[†] Email address for correspondence: jose.manuel.lopez.alonso@upc.edu

the inner cylinder is rotated, this system provides one of the best known examples of a supercritical transition to the turbulence (Coles 1965; Fenstermacher, Swinney & Gollub 1979). When the rotation speed exceeds a critical value, the initial purely azimuthal flow, known as circular Couette flow (CCF), becomes unstable due to a centrifugal instability, leading to a stationary axisymmetric pattern of toroidal vortices known as Taylor vortex flow (TVF) (Taylor 1923). As the rotation speed increases, the TVF is gradually replaced by flows of increasing spatio-temporal complexity, giving rise eventually to a fully turbulent state. The characteristics of the transitions and flow regimes that precede the onset of turbulence depend on the geometry of the system (i.e. the curvature and the length-to-gap aspect ratio). However, when the curvature is moderate, as is the case in most experiments, the route to chaos involves a series of Hopf bifurcations, i.e. the so-called Ruelle–Takens scenario (Ruelle & Takens 1971). The physical mechanisms underlying these transitions, as well as the spatial and temporal properties of the pre-turbulent flow regimes, have been widely investigated over decades and are now relatively well understood (Jones 1981; Gorman & Swinney 1982; King *et al.* 1984; Marcus 1984*a,b*; Jones 1985; Andereck, Liu & Swinney 1986; Hegseth, Baxter & Andereck 1996; Wereley & Lueptow 1998; Martinand, Serre & Lueptow 2014; Dessup *et al.* 2018).

This archetypal transition scenario, as well as the properties of the eventual turbulent state, are, however, substantially modified when long chain polymers (even in small amounts) are added to the working fluid. Unlike Newtonian fluids, the response of dilute polymer solutions to the flow stresses is not only a function of the strain, but also of the strain rate. This time-dependent behaviour of the fluid properties, known as viscoelasticity, often causes dramatic changes in the stability and spatio-temporal characteristics of the flow with respect to those of the Newtonian case. The most striking manifestation of this phenomenon is the occurrence of flow instability in the absence of inertia (Muller, Larson & Shaqfeh 1989; Larson, Shaqfeh & Muller 1990). This instability results from the combined effect of elasticity and curvature and produces different flow regimes depending on the elasticity level of the working fluid. When the elasticity level is moderate, the instability leads to a steady vortex pattern similar to the TVF (Baumert & Muller 1995, 1997; Al-Mubaiyedh, Sureshkumar & Khomami 1999). However, when the solution is highly elastic, the flow exhibits a form of chaotic motion dubbed elastic turbulence (Groisman & Steinberg 2000, 2004).

In parameter regimes where inertial effects are not negligible, the interplay between elasticity and inertia leads to a rich variety of flow patterns and spatio-temporal behaviours. The regions of existence of the different flow regimes in the parameter space defined by the elasticity level and the rotation speed (normally quantified by the dimensionless elasticity and Reynolds numbers, El and Re , respectively) are very sensitive to the experimental protocols and the polymer properties. Particularly significant among these properties is the shear thinning behaviour of the dilute polymer solution. Recent experiments have shown that strong shear thinning may even fully suppress elasto-inertially induced flow regimes (Cagney, Lacassagne & Balabani 2020; Lacassagne, Cagney & Balabani 2021). In cases where elastic effects prevail over shear thinning effects (e.g. Boger-like fluids), experiments and simulations have reported a number of flow regimes. These can be roughly divided into coherent and chaotic flow states. The most characteristic examples of coherent states are the so-called ribbons (RB), diwhirls (DW) and oscillatory strips (OS) (Groisman & Steinberg 1996, 1997; Baumert & Muller 1999; Crumeyrolle, Mutabazi & Grisel 2002; Thomas, Sureshkumar & Khomami 2006; Thomas, Khomami & Sureshkumar 2009). The RB arise from a supercritical Hopf bifurcation of the CCF at low Re values and consist of a rotating standing wave pattern formed by two spiral waves propagating axially in opposite senses. In contrast, DW and OS emerge from

nonlinear instabilities (in many cases as secondary instabilities of the RB pattern) and are vortex pairs characterized by strong inflows, which are confined within narrow axial regions, and weak outflows, which extend over axial distances that are usually three or four times larger than those of the inflows. The difference between DW and OS is that, whereas the former are stationary, the latter are oscillatory. Both these structures have the ability to merge when they are close to each other and usually appear as spatially localized states (Groisman & Steinberg 1997). The regimes of chaotic motion can be achieved either from the nonlinear development of these coherent flow patterns or directly from CCF via subcritical transition. The most typical examples of chaotic dynamics are disorder oscillations, spatio-temporal intermittency and flame-like turbulence (Groisman & Steinberg 1996; Baumert & Muller 1997, 1999; Thomas *et al.* 2006, 2009; Latrache, Crumeyrolle & Mutabazi 2012; Liu & Khomami 2013). Ultimately, when the rotation speed becomes sufficiently large, the flow reaches a state of highly disordered motion involving a wide range of spatial and temporal scales. This state is known as elasto-inertial turbulence (EIT) and it exhibits structural and statistical features which are markedly distinct from those of ordinary Newtonian turbulence (Liu & Khomami 2013; Song *et al.* 2019, 2021a).

In recent years, there has been a surge of interest in investigating the distinct pathways followed by the flow to achieve the EIT state. Experimental studies have so far identified three main types of transition scenarios. In the first type, dubbed defect-mediated (DM) transition (Latrache *et al.* 2012, 2016), the route to EIT starts when the state of RB undergoes a Benjamin–Fair instability which produces spatio-temporal defects in the flow pattern. The number of defects grows as Re increases, creating increasingly large regions of irregular spatio-temporal behaviour. This results first in a regime of spatio-temporal intermittency and subsequently in a fully chaotic flow that was identified as EIT. The DM transition takes place at low-to-moderate El values ($El < 0.15$) and Re values quite below those at which the onset of TVF happens in the Newtonian case. The second type of transition, known as transition via flames (Latrache & Mutabazi 2021), occurs at similar Re but larger El values ($0.15 \leq El \leq 0.3$). Again, the transition is initiated from the RB pattern, which in this case undergoes an instability that results in the emergence of flame-like structures. These flames proliferate as the rotation speed increases, increasing progressively the spatio-temporal complexity of the flow until the EIT regime is achieved. The third transition scenario is dubbed the vortex merging and splitting (VMS) transition (Lacassagne *et al.* 2020). Unlike the two previous transitions, the VMS occurs at Re values where CCF is centrifugally unstable and the primary instability results in a steady axisymmetric vortex flow that the authors identified as a TVF. Here, the spatio-temporal complexity of the flow increases following a temporal sequence of events in which the vortex pairs may be either annihilated or created. The frequency with which these events occur increases with increasing Re , giving rise eventually to a highly chaotic dynamics consistent with a EIT state.

While the experiments have shown that this VMS dynamics is of an elastic nature (Lacassagne *et al.* 2020), the reasons why axisymmetric vortex pairs undergo merging and splitting processes and why they occur at relatively high El levels are not known. This paper aims to shed some light on these aspects. Numerical simulations of viscoelastic TCF, using the FENE-P model to simulate polymer effects, are used to study the progressive transformation that the vortex flow pattern undergoes as El increases from the Newtonian limit ($El = 0$) up to El values well beyond the onset of the VMS dynamics. In contrast to what was thought, the simulations reveal that the VMS dynamics is not associated with a centrifugally driven TVF-like pattern, but with an elastically induced pattern of steady DW that fully replaces the TVF pattern at $El \approx 0.12$, where the instability mechanism changes

from being centrifugal to being elastic. These elastic vortices have a striking feature that had not been previously reported: the amount of angular momentum they carry decreases with increasing El . It is shown that the VMS dynamics starts when El is sufficiently large so that the contribution of these vortices to the angular momentum flux reaches a marginal level. The distinct vortex pairs become then dynamically disconnected from the rest of the system and begin to travel independently in the axial direction, creating the complex spatio-temporal dynamics characteristic of the VMS regime.

2. Problem formulation, dimensionless parameters and numerical methods

We consider the motion of a dilute polymer solution confined to the gap between two vertical, rigid and concentric cylinders of height h and radii r_i and r_o . Hereafter, the subscripts i and o denote the inner and outer cylinders, respectively. The inner cylinder rotates with an angular velocity, Ω_i , whereas the outer cylinder is at rest, i.e. $\Omega_o = 0$. The dynamics of this incompressible viscoelastic fluid flow is governed by the continuity and Navier–Stokes equations, along with an equation to describe the temporal evolution of a polymer conformation tensor, \mathbf{C} , which contains the ensemble average elongation and orientation of all polymer molecules in the flow. A simple Hookean dumbbell model is used to represent the polymer molecules (Bird, Dotson & Johnson 1980). Normalizing the velocity with the inner cylinder velocity, $\Omega_i r_i$, the length with the gap size, $d = r_o - r_i$, the pressure with the dynamic pressure, $\rho(\Omega_i r_i)^2$, where ρ is the fluid’s density, and the polymer conformation tensor with kT_e/H , where k denotes the Boltzmann constant, T_e is the absolute temperature and H is the spring constant, the dimensionless equations read

$$\left. \begin{aligned} \nabla \cdot \mathbf{v} &= 0, \\ \partial_t \mathbf{v} + \mathbf{v} \cdot \nabla \mathbf{v} &= -\nabla P + \frac{\beta}{Re} \nabla^2 \mathbf{v} + \frac{(1-\beta)}{Re} \nabla \cdot \mathbf{T}, \\ \partial_t \mathbf{C} + \mathbf{v} \cdot \nabla \mathbf{C} &= \mathbf{C} \cdot \nabla \mathbf{v} + (\nabla \mathbf{v})^T \cdot \mathbf{C} - \mathbf{T}, \end{aligned} \right\} \quad (2.1)$$

where $\mathbf{v} = (u, v, w)$ is the velocity vector field in cylindrical coordinates (r, θ, z) , P is the pressure, $\beta = \nu_s/\nu$ indicates the relative importance between the solvent viscosity ν_s and the viscosity of the solution at zero shear rate ν and $Re = \Omega_i r_i d/\nu$ is the Reynolds number based on the inner cylinder velocity. Polymers are coupled to the Navier–Stokes equations through the polymer stress tensor \mathbf{T} , which is calculated using the FENE-P model (Bird *et al.* 1980),

$$\mathbf{T} = \frac{1}{Wi} \left(\frac{\mathbf{C}}{1 - \frac{tr(\mathbf{C})}{L^2}} - \mathbf{I} \right), \quad (2.2)$$

where \mathbf{I} is the unit tensor, $tr(\mathbf{C})$ is the trace of the polymer conformation tensor, L denotes the maximum polymer extension and Wi is the Weissenberg number, a dimensionless quantity that measures the ratio of the polymer relaxation time λ to the advective time scale $d/(\Omega_i r_i)$.

Experimental observations in Lacassagne *et al.* (2020) strongly suggest that the dynamics relevant to the VMS transition is two-dimensional and occurs in the meridional plane (r, z) . Based on this assumption, the simulations were conducted in a quasi-two-dimensional TCF system (i.e. under axisymmetric conditions), where the velocity field does not depend on the azimuthal coordinate, θ . This choice allows us to significantly reduce the cost of the simulations, making it possible to simulate

the viscoelastic flow for very long periods of time. Some simulations in a fully three-dimensional TCF system were also subsequently performed to verify that the dynamics found in the axisymmetric simulations persists in the full domain.

Periodic boundary conditions are used in the z direction, whereas the dimensionless boundary conditions at the cylinders are

$$\left. \begin{aligned} \mathbf{v}(r_i, z) &= (0, 1, 0), \\ \mathbf{v}(r_o, z) &= (0, 0, 0). \end{aligned} \right\} \quad (2.3)$$

The parameters used in the simulations have been chosen to mimic as closely as possible those in the experiments of Lacassagne *et al.* (2020). The curvature of the system is the same as in the experiments, $\eta = r_i/r_o = 0.77$, and all simulations have been performed at a constant value of the Reynolds number, $Re = 95$, consistent with the Re value at which the onset of complex spatio-temporal dynamics takes place in the experiments. It must be noted that, at this Re value, the laminar Couette flow is centrifugally unstable, and therefore the flow pattern in the Newtonian case consists of Taylor vortices (the onset of Taylor vortices occurs at $Re = 89$ for this value of η). The same concentration of polymers as in the experiments has been used, $\beta = 0.871$, and similar levels of the polymer elasticity, quantified by the elasticity number, $El = Wi/Re$, have also been considered.

There are, however, other parameters and features that could not be matched. The height-to-gap aspect ratio, $\Gamma = h/d$, in the simulations had to be reduced with respect to that in the experiments, $\Gamma = 21.5$, to keep the computational cost affordable. The majority of the simulations have been performed using $\Gamma = 12.6$. Simulations at other values of Γ , spanning between 9 and 16, have also been conducted to assess the influence of this parameter on the dynamics observed in the simulations (§ 3.5). Another difference with respect to the experimental set-up is the absence of endplates. While secondary flows resulting from the interaction between flow and endplates are known to often alter the stability properties and dynamics of Newtonian TCF (Czarny *et al.* 2003; Avila *et al.* 2008; Lopez & Avila 2017), Lacassagne *et al.* (2020) noted that this does not seem to be the case in their experiments. Hence, simulations in an axially periodic domain are expected to provide a good qualitative representation of the observed dynamics. Finally, another parameter that sets a difference with respect to the experiments is the maximum polymer extension L . This parameter of the FENE-P model is a property of the dilute polymer solution which cannot be easily inferred from the specifications of the polymer used in the experiments (polyacrylamide, Sigma-Aldrich, $M_w = 5.5 \times 10^6 \text{ g mol}^{-1}$). Most of the simulations presented in this paper have been conducted using $L = 100$, which is a standard value in the literature of viscoelastic TC flows (Liu & Khomami 2013; Song *et al.* 2019, 2021a). The influence of varying this parameter is analysed in the § 3.5, where simulations with L varying between 30 and 250 are presented and discussed.

To solve (2.1), we use our open source code nsCouette (López *et al.* 2020), which has been recently extended to simulate viscoelastic flows using the FENE-P model. This code is a highly scalable pseudo-spectral solver for annular flows that implements a very efficient hybrid parallelization strategy (see Shi *et al.* (2015), for details). The spatial discretization in the z direction is carried out via Fourier–Galerkin expansion, whereas high-order central finite differences on a Gauss–Lobatto–Chebyshev grid are used in r . A pressure Poisson equation formulation is used to decouple the pressure from the velocity field. The free divergence condition (i.e. the continuity equation) is enforced by using an influence matrix technique, so that this condition is satisfied up to machine error. The time integration was carried out using a second-order accurate predictor–corrector scheme based on the Crank–Nicolson method (Willis 2017). Further details about the time stepper

Γ	m_r	m_z
9	128	192
10	128	256
12.6	128	256
14	128	384
16	128	512

Table 1. Number of radial nodes (m_r) and axial Fourier modes (m_z) used in the simulations depending on the aspect ratio Γ of the system.

can be found in Lopez, Choueiri & Hof (2019). As customary in numerical simulations of viscoelastic flows using pseudospectral codes, a small amount of artificial diffusion is added to stabilize the integration. The necessity to include this diffusion arises from the hyperbolic nature of the time evolution equation for \mathbf{C} . The absence of a diffusive term in this equation leads to an accumulation of numerical error that in many cases results in numerical breakdown. To avoid this problem, a Laplacian term, $(1/ReS_c)\nabla^2\mathbf{C}$, is added to the right-hand side of that equation, where the Schmidt number, $S_c = \nu/\kappa$, quantifies the ratio between the viscous and artificial diffusivities. In the simulations presented here, $S_c = 100$, which yields an artificial diffusion coefficient, $1/ReS_c = 10^{-4}$. This amount of diffusion is similar in magnitude to those used in other recent numerical studies on viscoelastic flows (Xi & Graham 2010; Lopez *et al.* 2019; Song *et al.* 2019; Zhu *et al.* 2020; Song *et al.* 2021b; Zhu *et al.* 2022). It has been verified that a reduction in the amount of diffusion does not significantly alter the results of the simulations (S_c up to 200 were tested), thereby confirming the adequacy of the diffusion used for the simulations throughout the paper. Due to the addition of a Laplacian term, boundary conditions for \mathbf{C} are needed at the cylinders. To avoid introduction of artificial boundary conditions, the values of \mathbf{C} at the cylinders are obtained by solving its evolution equation without the artificial diffusion term. This strategy was first introduced by Beris & Dimitropoulos (1999) and it has been widely used since then. The number of radial nodes and Fourier modes used in the computations are shown in table 1 for the different values of Γ considered. The time step size had to be varied between 4×10^{-3} and 10^{-3} as the polymer elasticity (i.e. El) was increased.

3. Results

3.1. Transition to the VMS regime with increasing El

We first investigate the gradual approach to the VMS regime as the elasticity of the fluid increases. For this initial simulation, an aspect ratio of $\Gamma = 12.56$ was considered, whereas the maximum polymer extension was set to $L = 100$. A Newtonian simulation (i.e. $\beta = 1$) was initially run to calculate a TVF pattern with six pairs of counter-rotating vortices. Using this state as initial condition, the fluid's elasticity was slowly and steadily increased at a uniform rate, $El = 10^{-3}t/Re$, until a dynamical regime characterized by merging and splitting events was found. We would like to stress that the protocol followed in this simulation differs from that in the experiments, where the VMS regime is achieved by increasing Re while keeping a constant elasticity (Lacassagne *et al.* 2020). Our study hence offers a different perspective into the pathway leading to this flow regime and allows to identify the gradual transformation the flow undergoes as the working fluid becomes more elastic.

Panel (a) in figure 1 provides an overview of the structural and dynamical changes induced by the polymers on the initial TVF as El increases. It shows a space–time diagram of the radial velocity u at mid-gap along the axial direction z , where time has been replaced by its corresponding El value. Red areas represent fluid motion from the inner to the outer cylinder, i.e. outflows, whereas blue regions indicate fluid moving from the outer to the inner cylinder, i.e. inflows. Panel (b) places emphasis in the range of El values for which a complex spatio-temporal dynamics happens. The stationary pattern of vortices becomes unstable at $El \approx 0.29$, leading to periodic oscillations of the vortex pairs along the z -axis. The onset of the VMS regime takes place soon after, at $El \approx 0.315$, as the dynamics of the distinct vortex pairs decouples and these begin to move independently in the axial direction. It will be shown later in §3.5 that this threshold is sensitive to the number of vortices of the initial condition and the aspect ratio used in the simulations. Merging events, where two vortex pairs coalesce to form a single vortex pair, are indicated as dashed (green) rectangles in figure 1(b). These events fully dominate the dynamics in the initial phase of the VMS regime (for $0.32 < El < 0.34$) and since they occur simultaneously at different axial locations, the total number of vortex pairs in the system rapidly decreases. After this initial phase ($El > 0.34$), merging events coexist with events where a vortex pair branches into two, i.e. splitting events, shown as dash-dotted (purple) rectangles in the figure, as well as with regions where the dynamics becomes transiently chaotic (see for instance the flow region between $4 < z/d < 7$ for $0.34 < El < 0.36$ or $0 < z/d < 2.5$ for $0.38 < El < 0.40$). The number of vortex pairs fluctuates between two and four in this phase.

It is important to note that the occurrence of VMS events does not depend on the continuous increase of El with time. If El is held constant after the VMS regime is achieved, the simulations show the same dynamic events just described: vortex merging, vortex splitting and transient chaotic motion, reflecting that these are temporal characteristics of the flow that occur when El exceeds a certain critical threshold. This is demonstrated in figure 1(c), which shows a space–time map for a simulation where El has been fixed to 0.32. Interestingly, the VMS events observed in simulations with constant El are similar to those observed in simulations where El varies with time. The reason (which will be discussed later in the paper) is that increasing El has little influence on the vortices in this flow regime. As a result, space–time diagrams corresponding to simulations where El changes with time not only feature the various flow regimes obtained when El is varied but also provide an accurate representation of the VMS events.

Another important feature that is clearly illustrated in figure 1(a) is the strong impact that increasing El has on the structure of the vortex pairs. We anticipate here that these structural changes are key to understanding the physics underlying merging and splitting events. Hence, before getting into detail about the dynamics in the VMS regime, it is convenient to present a comprehensive study about the influence of elasticity on the TVF.

3.2. Viscoelastic modification of the TVF

A well-known property of viscoelastic flows with curved streamlines is the appearance of a radially inward force which is caused by the elastic stresses arising from the stretching of the polymer molecules by the primary flow (Groisman & Steinberg 1998). This force has been identified as the driving source of a number of instabilities in curvilinear flows of highly elastic polymer solutions, which are usually known as purely elastic instabilities (Shaqfeh 1996). The mechanism underlying these instabilities has been discussed in detail and verified in many studies, particularly in flow regimes where inertial effects are negligible ($Re \rightarrow 0$). It is, however, reasonable to expect that this elastic force will

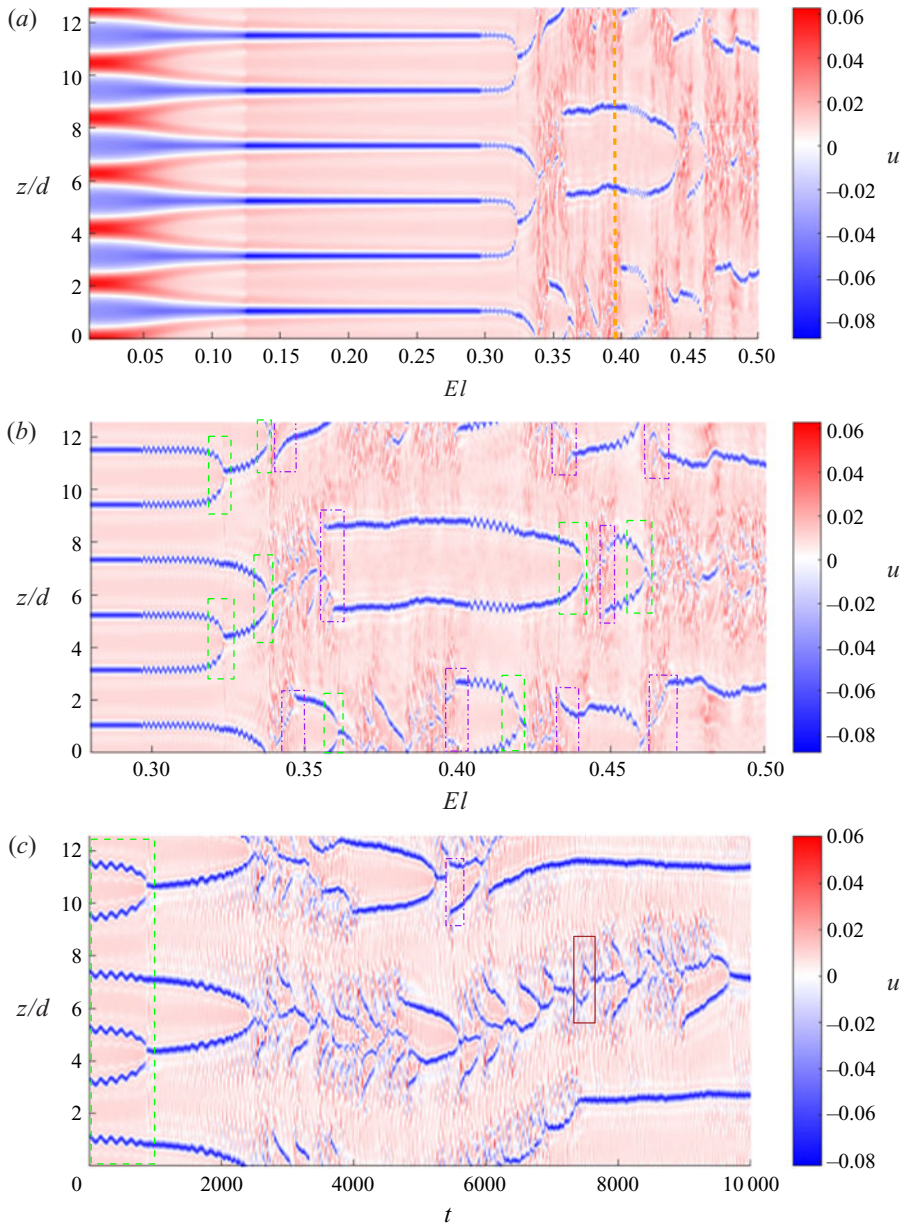


Figure 1. Space–time plot representing the magnitude of the radial velocity u at mid-gap along the axial direction z . Panels (a) and (b) correspond to a simulation performed at $Re = 95$ where, starting from a Newtonian TVF, El was slowly increased with time ($El = 10^{-3}t/Re$). Note that the time t has been replaced by the corresponding El values on the horizontal axis. Panel (a) shows the variation of u from Newtonian flow (i.e. $El = 0$) up to the largest El value simulated ($El = 0.50$), whereas panel (b) shows in more detail the range of El values for which a complex spatio-temporal dynamics take place. Panel (c) illustrates the spatio-temporal dynamics when El is kept constant after the VMS regime is achieved. The case exemplified corresponds to $El = 0.32$. Red and blue areas indicate outflows and inflows respectively. Note that periodic boundary conditions are used in z .

Vortex merging and splitting events in viscoelastic TCF

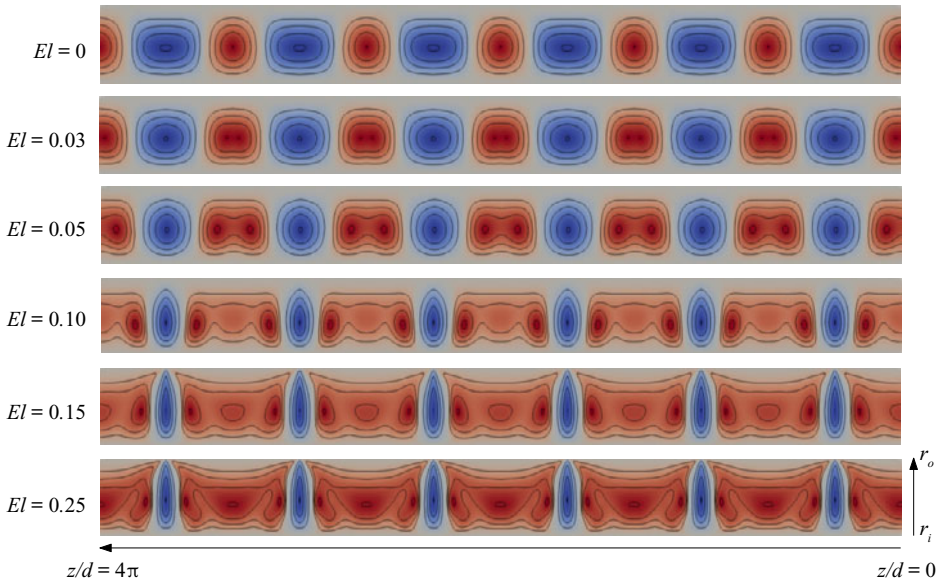


Figure 2. Structural variation of the TVF pattern as El increases from the Newtonian case (i.e. $El = 0.00$) up to values near the onset of spatio-temporal dynamics. Each panel shows a colour map of the radial velocity u in a meridional plane $(z/d, r/d) \in [0, 4\pi] \times [3.35, 4.35]$, where red regions indicate outflows (i.e. positive velocity), blue regions represent inflows (i.e. negative velocity) and the zero velocity has been set as grey. The colour scale is based on the maximum and minimum values of each case and hence differs among the different panels. There are four positive and four negative contours evenly distributed across the full range of values in each case: 1. $El = 0.00$, u in $[-0.037, 0.059]$; 2. $El = 0.03$, u in $[-0.043, 0.047]$; 3. $El = 0.05$, u in $[-0.048, 0.029]$; 4. $El = 0.10$, u in $[-0.048, 0.014]$; 5. $El = 0.15$, u in $[-0.082, 0.015]$; 6. $El = 0.25$, u in $[-0.072, 0.011]$. The system is shown rotated by 90° in the counterclockwise direction with respect to its original position. The location of the inner and outer cylinders, r_i and r_o , respectively, as well as the locations of the top ($z/d = 4\pi$) and bottom ($z/d = 0$) of the system are indicated in the bottom panel.

also have an influence in parameter regimes where Newtonian flows become unstable due to inertial forces. The stationary pattern of Newtonian Taylor vortices used as starting solution in our calculations is one such case: it arises from a centrifugal instability of the purely azimuthal primary flow (Taylor 1923). This instability mechanism is expected to persist in the viscoelastic case as El is slowly increased starting from the Newtonian limit. However, the structure of the Taylor vortex pattern is likely to be modified by the competition between the centrifugal and elastically induced forces. Additionally, if the fluid's elasticity becomes sufficiently large, the elastic instability mechanism might replace the centrifugal mechanism, leading to a flow state that is elastic in nature but whose structure could be modified by the presence of inertial effects. In this section we show that this is indeed the case in our simulations.

Figure 2 shows colour maps of the radial velocity, u , illustrating the dependence of the flow structure as El increases from the Newtonian limit ($El = 0$) up to the regime in which the flow exhibits spatio-temporal behaviour. Note that, to save space, in all figures illustrating flow patterns throughout the paper, the system is shown rotated by 90° in the counterclockwise direction, so that the inner (outer) cylinder is located at the bottom (top) of each panel and the positive z -direction goes from right to left (see the coordinate system in the bottom panel of figure 2). The structure of the TVF pattern in the Newtonian case (top panel) shows a small asymmetry between outflows and inflows, as the axial extent of the inflows is slightly greater than that of the outflows. This characteristic fully reverses

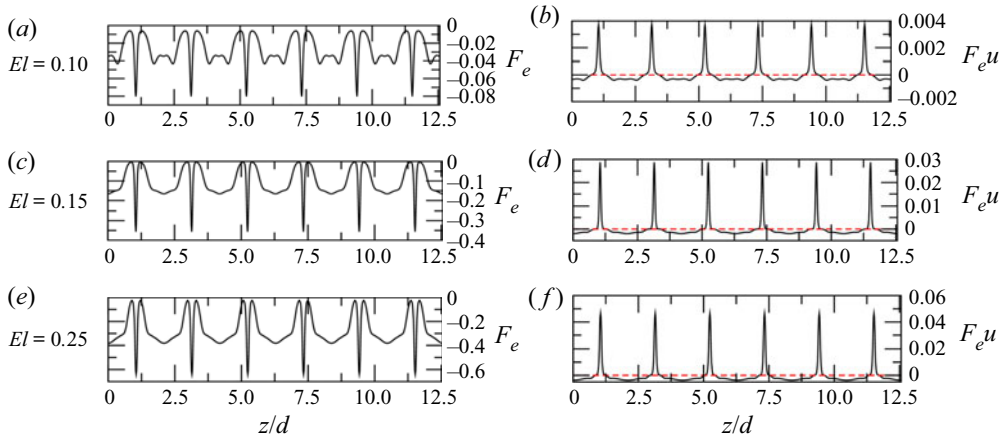


Figure 3. Axial profiles of the elastic force F_e (left panels) and its associated work $F_e u$ (right panels) obtained at the mid-gap for El values matching those of the last three panels in figure 2. The elastic force is calculated as $F_e = ((1 - \beta)/Re)(\partial_r T_{rr} + (T_{rr} - T_{\theta\theta})/r + \partial_z T_{rz})$. A dashed line has been added at $F_e u = 0$ to help identify inflows ($F_e u > 0$) and outflows ($F_e u < 0$).

as elasticity comes into play. The axial extent of the inflows decreases with increasing El and these become eventually confined to strong jets that extend over narrow regions in the axial direction. Conversely, the axial extent of the outflows increases notably (note that they become nearly four times larger than the inflows for $El \geq 0.12$) and the magnitude of u in these regions decreases substantially as El increases (the range of values of u corresponding to each panel is specified in the caption).

It was postulated in a previous experimental study that this strong asymmetry between inflows and outflows might be caused by the work done by the elastically induced force (Groisman & Steinberg 1998). To verify this hypothesis quantitatively, figure 3 shows axial profiles of the elastic force, hereafter denoted as F_e (panels *a, c, e*), and its associated work $F_e u$ (panels *b, d, f*), obtained at the mid-gap for the last three cases shown in the figure 2. As seen, the profiles of F_e are always negative, reflecting that F_e is an inward force, and they exhibit strong peaks in the inflows whose magnitude increases with increasing El . Since F_e acts in the same direction as u in the inflows, it does positive work on the flow in these regions. This circumstance implies that the strong peaks of F_e will result in large positive work (see the peaks of $F_e u$ in panels *b, d, f*), which enhances the fluid motion in the inflows and creates the strong localized jets that appear as El increases. In the outflows, on the contrary, F_e acts in opposition to the fluid motion and therefore does a negative work on the flow. This characteristic explains the decay in the magnitude of u that is observed in the outflows as El increases. The axial extent of the inward jets decreases as the magnitude of the peaks grows, which evidently entails an increase in the axial extent of the outflows and creates the asymmetry between inflows and outflows observed in figure 2.

In addition to the emergence of this asymmetry, a second transformation takes place inside the outflows. The region where the largest positive velocity occurs, which in the Newtonian case is located at the centre of the outflows, separates in the viscoelastic cases into two identical regions which are symmetric with respect to the central symmetry plane of the outflow. These new regions of maximum positive velocity move away from each other as El increases and approach progressively the adjacent inflows. When the elasticity is sufficiently large ($El \geq 0.12$), the strong inflow jets are flanked by these regions of

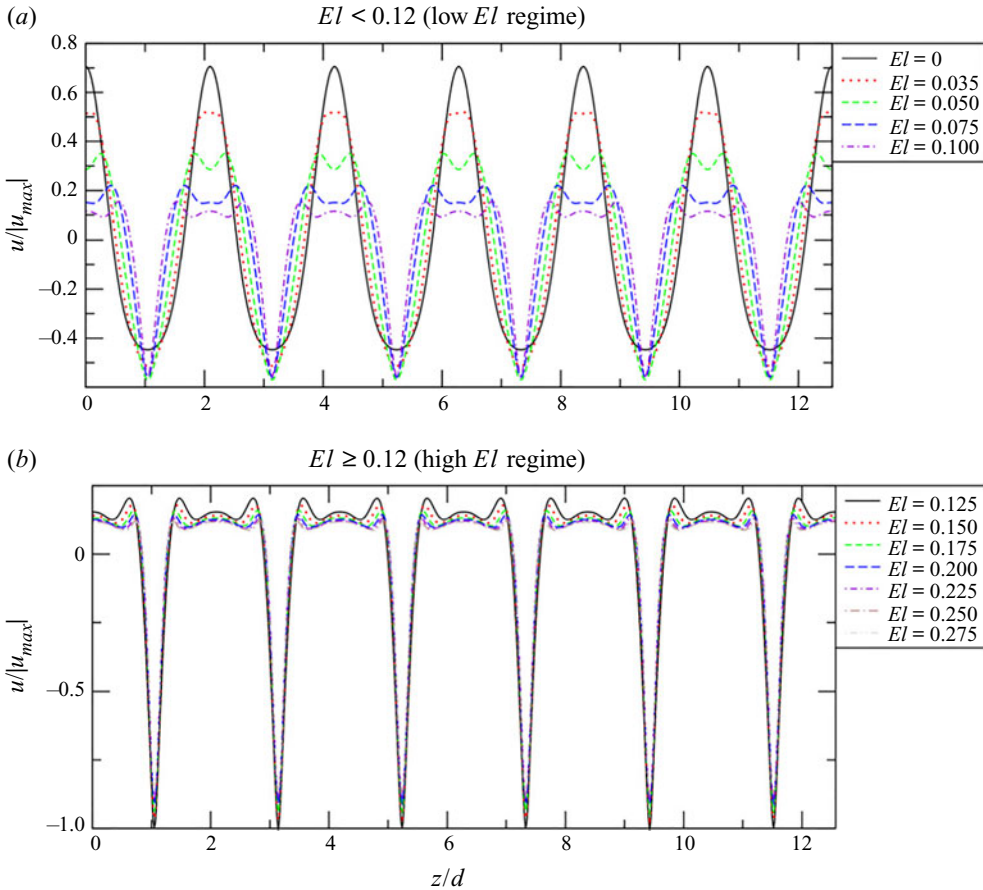


Figure 4. Profiles of the radial velocity u at mid-gap along the z -axis. Panel (a) shows profiles for $El < 0.12$, where profound changes in the structure of the flow pattern are observed in figure 2, whereas panel (b) focuses on the range of El values ($El \geq 0.12$) where the variation in the profiles is small. Note that in both panels u is normalized with the largest absolute value among all cases which is obtained for $El = 0.12$ and corresponds to $|u_{max}| = 0.0824$.

maximum positive velocity, whereas the flow in the central part of the outflows becomes nearly uniform in the axial direction.

A remarkable feature of this structural transition is the fact that the changes are most pronounced in the low El regime ($El < 0.12$). This observation is quantitatively confirmed by the axial profiles of u at the mid-gap shown in figure 4. Profiles corresponding to $El < 0.12$ (shown in panel (a)) differ markedly and clearly reflect strong changes in both the magnitude of u (particularly in the outflows) and the axial extent of inflows and outflows. However, for $El \geq 0.12$ (see panel (b)), the differences among profiles are small and mainly occur in the magnitude of u , which keeps slightly decreasing (increasing) in the outflows (inflows) with increasing El . Further quantitative evidence of this behaviour is given in figure 5. Panel (a) in this figure shows the dependence of the axial extent of the inflow and outflow regions at the midgap with increasing El . It is apparent that the largest variation in the extent of these regions (which are naturally inversely proportional) occur within the low El regime, for $0.05 < El < 0.1$. Likewise, the sharpest change in the ratio between the maximal velocity of outflows and inflows (shown in panel (b)) also happens at very low El

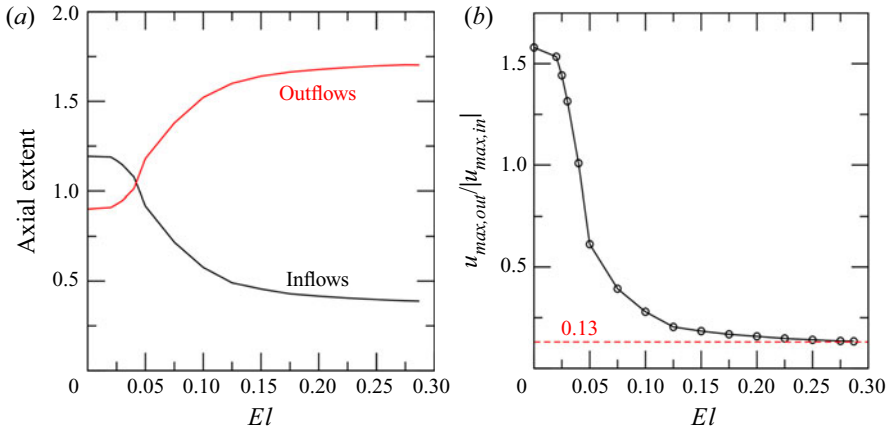


Figure 5. Quantification of the changes in the structure and strength of the vortices as El increases. Panel (a) shows the variation in the axial extent of inflows and outflows at the midgap in units of the gap-width, d , as the fluid becomes more elastic. Panel (b) displays the ratio between the maximal values of u in the outflows and inflows as a function of El . The dashed line indicates the approximate value this ratio seems to approach asymptotically as El increases.

values ($El < 0.05$), where the strength of the outflows decays strongly. These observations clearly evidence that F_e exerts a surprisingly strong influence on the flow structure even in weakly elastic fluids. Another interesting feature revealed by the two panels of figure 5 is that the flow characteristics appear to exhibit asymptotic behaviour. As El increases, the sizes of the outflows and inflows approach values close to $L_{out}/d \approx 1.7$ and $L_{in}/d \approx 0.38$, respectively, whereas the ratio between the maximal velocities in outflows and inflows appears to level off at approximately 0.13. This observation is also corroborated by the velocity profiles, which seem to be gradually converging with increasing El (see panel (b) in figure 4).

An important distinction between the low and high El regimes (i.e. $El < 0.12$ and $El \geq 0.12$) is the magnitude of u in the inflows. As seen in figure 4(a), the maximum velocity of the inflows in the low El regime increases initially with increasing El , but eventually converges to a value close to $u/|u_{max}| = -0.55$. This value is substantially lower than those shown by the profiles in the high El regime (see figure 4b), where $u/|u_{max}|$ ranges from -1 at $El = 0.125$ (when it is maximal) to ~ -0.78 at $El > 0.25$ (when the profiles seem to converge). The transition between both regimes can be clearly identified in the space–time plot of figure 1(a) as a sudden change in the colour intensity that takes place at $El \sim 0.12$. The abrupt nature of this transition strongly suggests that it may be caused by a change in the physical mechanism associated with the instability of the primary flow. To test this hypothesis we examine the integral energy budgets. For viscoelastic flows, the energy balance reads (Dallas, Vassilicos & Hewitt 2010; Dubief, Terrapon & Soria 2013),

$$\int_V \mathcal{P} dV - \int_V \epsilon dV - \int_V \Pi_e dV = 0, \quad (3.1)$$

where \mathcal{P} is the kinetic energy production, ϵ is the viscous dissipation rate and Π_e denotes the work done by the elastic stresses. These quantities were calculated using the following expressions:

$$\mathcal{P} = -\overline{u'v'} \frac{\partial \bar{v}}{\partial r} + \overline{u'v'} \frac{\bar{v}}{r}, \quad (3.2)$$

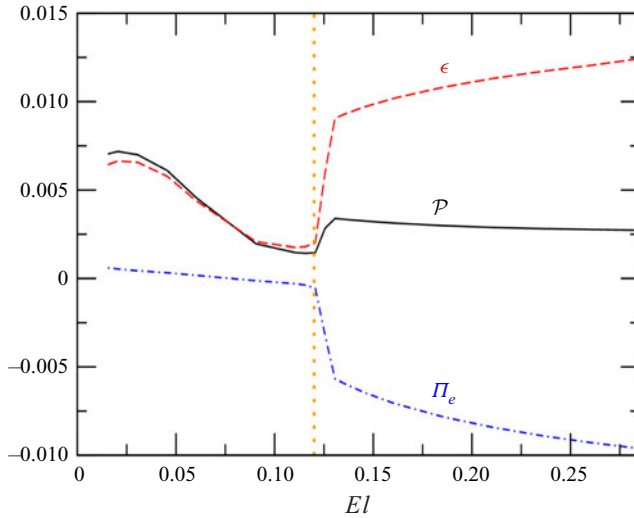


Figure 6. Variation of the integral energy budgets with increasing El before the spatio-temporal dynamics sets in. Here, \mathcal{P} denotes the kinetic energy production by the inertial forces, ϵ stands for the viscous dissipation and Π_e is the work done by the elastic stresses. The dotted (orange) vertical line indicates the El value at which the transition between the low and high El regimes takes place. Hereafter, these regimes are denoted as centrifugally and elasticity dominated regimes, respectively.

$$\epsilon = \frac{2\beta}{Re} \overline{\mathbf{S}' : \mathbf{S}'}, \quad (3.3)$$

$$\Pi_e = \frac{1 - \beta}{Re} \overline{\mathbf{S}' : \mathbf{T}'}. \quad (3.4)$$

Here, the overline denotes axially averaged quantities, $\mathbf{S}' = (\nabla \mathbf{v}' + \nabla \mathbf{v}'^T)/2$ is the rate of strain tensor and the prime symbol indicates deviations of the velocity or polymer stress tensor from their axially averaged values ($\bar{\mathbf{v}} = (0, \bar{v}, 0)$ and $\bar{\mathbf{T}}$). It must be clarified that, although this equation was derived in the context of turbulent flow, it also applies to steady and axisymmetric vortex flow (the derivation of the equation for this particular case is given in [Appendix A](#)). The first and second integrals in (3.1) are always positive, meaning that they act as source and sink terms of the energy balance, respectively (note that there is minus sign in front of the second integral). The sign of the third integral can be positive or negative. If it is positive, this term has a negative contribution to the balance and thus polymers act to dissipate the fluid's kinetic energy. By contrast, if it is negative, polymers act as an energy source. The variation of the values yielded by these integrals with increasing El is shown in [figure 6](#). As expected, the behaviour of the polymers changes drastically at $El \sim 0.12$, consistent with the transition between the low and high elasticity regimes. At low El values, polymers play a dissipative role, helping the viscous forces to damp the centrifugally induced vortices. However, at $El \sim 0.1$, the work done by the elastic stresses changes sign and the net contribution of the polymers to the energy balance becomes positive, indicating that they inject energy into the flow through the elastic stresses. The amount of energy that the polymers supply to the system is initially very small (for $0.1 \leq El < 0.12$) but increases suddenly when $El \sim 0.12$. After this transition occurs, the energetic contribution of the polymers becomes the dominant energy source and its magnitude continues increasing with increasing El . In contrast, the energy production due to inertial mechanisms remains small and decreases very gradually

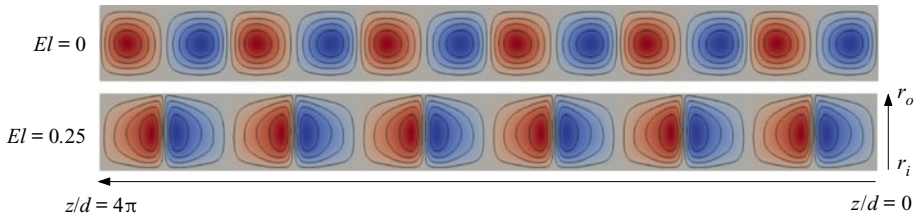


Figure 7. Comparison between the flow streamlines ψ in the centrifugally (top) and elastically (bottom) dominated regimes. Positive (negative) values are represented as red (blue), whereas the zero value is shown as grey. The colour scale is based on the maximum and minimum values of each case and hence differs between the panels. There are four positive and four negative contours evenly distributed across the full range of values in each case: 1. $El = 0.00$, ψ in $[-0.660, 0.660]$; 2. $El = 0.25$, ψ in $[-0.295, 0.295]$. The system is shown rotated by 90° in the counterclockwise direction.

as El increases. From this analysis, it is clear that the nature of the mechanism driving the instability indeed changes from being centrifugal ($El < 0.12$) to being elastic ($El \geq 0.12$), a characteristic that sets a clear distinction between the two regimes investigated so far.

Finally, to facilitate comparison between the flow structure in the high El regime and other elastically induced stationary patterns previously reported, the streamlines of the flow ψ at $El = 0.25$ are shown in the bottom panel of figure 7. These are naturally very different from those in the Newtonian case (also shown for comparison in the top panel) and reflect again the structural changes just discussed. As seen, unlike the Newtonian case, where the vortices are nearly equidistant, in the elastically dominated regime they appear to be arranged in pairs, with their cores being located very close to one another. We note that this type of structure has been previously reported in the literature and it is usually known as DW (Groisman & Steinberg 1997; Lange & Eckhardt 2001; Thomas *et al.* 2006, 2009), due to its similarity to the shape of a magnetic dipole. However, there are a couple of important differences between the structures described in previous works and the one presented here. A characteristic shared by all previous studies is that DW appear after a hysteretic transition, when Re is decreased starting from a flow state driven by an elastic instability. In fact, it is often stated in the literature that flow deceleration is a necessary condition to observe these structures (Groisman & Steinberg 1997; Lange & Eckhardt 2001; Thomas *et al.* 2006; Lacassagne *et al.* 2020). The present study shows that this is not the case and that, at least in the regime investigated here, these structures may also appear for a fixed Re if the elasticity of the working fluid is sufficiently large so that the elastic instability mechanism replaces the centrifugal mechanism. In the low Re regimes where most previous studies were conducted, DW appear to be localized in the axial direction, i.e. there are regions where the flow is laminar interspersed between distinct DW. When the distance between DW becomes less than $5d$, they approach each other and coalesce. This characteristic is so far absent in the present simulation. Despite the distance between DW being substantially lower than $5d$, they remain stationary and form a pattern of equally spaced structures along the axial direction. A possible reason for such difference will be discussed later in § 3.6. We would like to finally note that similar arrangements of DW, yet not stationary, have also been reported in the literature, which were dubbed OS (Groisman & Steinberg 1996; Thomas *et al.* 2006, 2009).

3.3. Onset of spatio-temporal dynamics

The stationary pattern of DW loses its stability at a Hopf bifurcation which takes place at $El \sim 0.29$ leading to an axial oscillation of the vortices. This is illustrated in figure 8

Vortex merging and splitting events in viscoelastic TCF

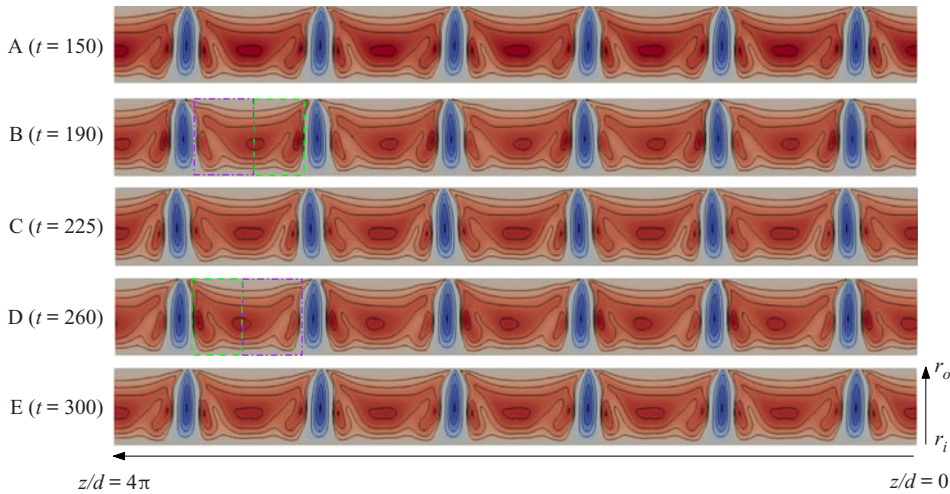


Figure 8. Colour maps of u illustrating the axial oscillation of the vortex pairs that emerges from the Hopf bifurcation. Letters from A to E are used to show the correspondence between each panel and the time series shown in figure 9. Positive (negative) velocity is represented as red (blue), whereas the zero velocity is shown as grey. There are four positive and four negative contours evenly distributed in $u \in [-0.0780, 0.0095]$. The system is shown rotated by 90° in the counterclockwise direction. Note that the flow patterns shown in A and E are identical, whereas those shown in B and D only differ in that their outflows are antisymmetric.

through colour maps of u taken at five equally spaced time instants within a period (shown as circles in figure 9a). The displacement of the vortices is relatively small, yet clearly discernible in the figure by looking at the axial position of the inflows. It should be recalled that the system is shown rotated by 90° counterclockwise, and so the upwards (downwards) motion of the inflows corresponds to leftwards (rightwards) motion in these figures. Starting from the state where the inflows are at their lowest axial positions (panel A), it is observed that the inflows move first axially upwards (panel B), reach the position of maximum displacement (panel C) and subsequently move downwards (panel D), returning eventually to the initial state (panel E, which is identical to A). A notable difference with respect to the stationary case is the breakdown of the symmetry in the outflows. When the vortices move axially upwards, the lower half of the outflow (see region enclosed by the (green) dashed rectangle in the panel B) remains similar to that in the stationary case (see bottom panel in figure 2), however, the upper half (marked by the purple dash-dotted rectangle in panel B) notably changes due to an increase in the maximal velocity next to the inflow. The opposite is observed when the vortices move downwards. The upper half (shown as a green dashed rectangle in panel D) of the outflow remains as in the stationary case, whereas the lower half (purple dash-dotted rectangle in panel D) takes a similar form to that of the upper half during the upward motion. As a consequence, flow states moving axially upwards and downwards, where the vortices are located at the same axial positions, exhibit antisymmetric outflows (that is the case, for example, for states B and D shown in the figure).

The frequency of the oscillation was determined by applying fast Fourier transform to a time series of the axial velocity w obtained at a radial location close to the outer cylinder (figure 9a). The power spectral density is shown in figure 9(b), where the frequency is normalized with the elastic frequency, f_e . Following Lacassagne *et al.* (2020), f_e was calculated as $f_e = 2c_e/k_{avg}$, where c_e denotes the wave celerity, $c_e = \sqrt{\nu/\lambda}$, and k_{avg} is the average spatial wavelength of the vortex flow pattern. The spectrum shows a pronounced

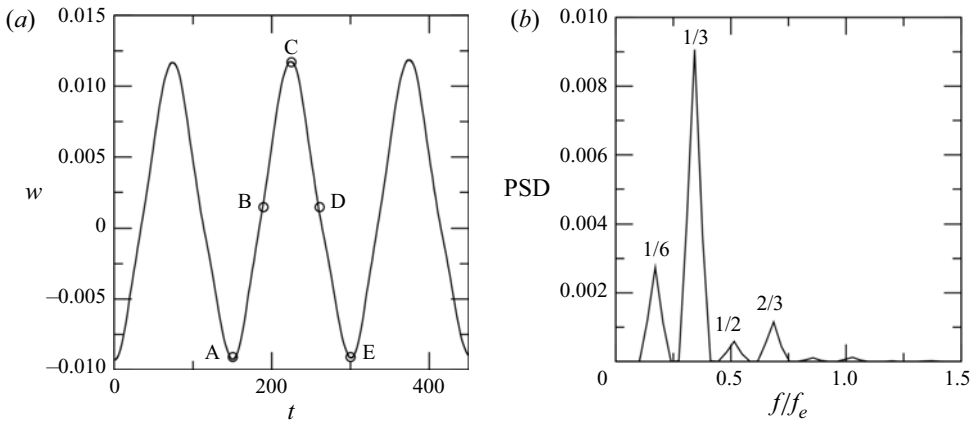


Figure 9. Periodic motion arising from the instability of the stationary pattern of DW. (a) Time series of the axial velocity w for $El = 0.3$ calculated at $r/d = 4.15$ and $z/d = \pi$. The circles indicate time instants for which colour maps of u are presented in figure 8. (b) Power spectral density (PSD). The frequency is normalized with the elastic frequency, f_e .

peak at $f_e/3$, which clearly indicates that this is the dominant frequency of the oscillation. Other peaks with smaller amplitudes are also observed. However, they correspond in all cases to other sub-harmonics of f_e and are therefore commensurate with the dominant frequency. It should be noted that $f_e/3$ is the dominant frequency for the particular case where the flow pattern has six vortex pairs. For other flow patterns with different numbers of vortex pairs, the oscillation is characterized by other subharmonics of f_e . The fact that frequencies appear in the spectrum as subharmonics of f_e is in full agreement with the experimental observations (Lacassagne *et al.* 2020) and reflects once again the elastic nature of the instabilities taking place at these El values.

From a mechanistic perspective, the periodic up and down motion of the vortices is just a consequence of the physics described in the previous section. The distance between the centres of the vortices on either side of the inflows keeps decreasing (albeit very gradually) as El increases, leaving a gap between DW where the radial velocity is increasingly weak. The axial velocity, whose role before the instability onset is simply to transport the fluid vertically near the cylinders (see top panel in figure 10), eventually penetrates into these intermediate regions, connecting adjacent vortices to each other in the outflow region and giving rise to an axial wave. This wave propagates first axially upwards (middle panel in figure 10) and subsequently reflects back and travels axially downwards (bottom panel in figure 10), thereby creating a standing wave. The interaction between standing wave and vortices lead to the axial oscillation of the latter illustrated above.

3.4. VMS dynamics

With a further increase in El , the dynamics of the different DW decouples and these begin to travel independently along the axial direction. A merging event happens when two DW move towards each other and eventually coalesce into a single entity. This phenomenon is illustrated in figure 11, which shows the variation of the radial velocity over the initial stage of the VMS regime in the simulation performed at constant $El = 0.32$. Two merging events occur simultaneously in the time window shown (corresponding to the green dashed rectangle in figure 1c). In the initial phase of the merging process (up to $t \approx 500$), the second and fifth DW starting from the top (indicated by black leftwards arrows) leave their

Vortex merging and splitting events in viscoelastic TCF

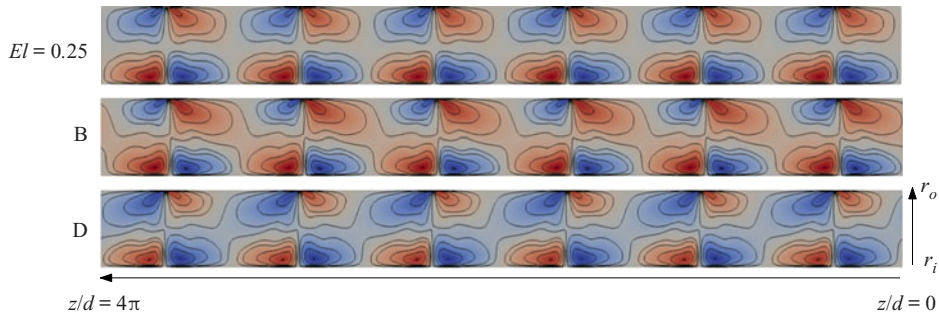


Figure 10. Colour maps of w illustrating the standing wave causing the axial oscillation of the flow pattern. The top panel shows w for a stationary state at $El = 0.25$, whereas the middle and bottom panels correspond to the states B and D indicated in figure 9. Positive (negative) values of w are shown as red (blue), whereas that for $w = 0$ is shown as grey. From top to bottom, there are four positive and four negative contours evenly distributed in $w \in [-0.030, 0.030]$, $[-0.026, 0.030]$ and $[-0.030, 0.026]$, respectively. Two additional contours at $w = \pm 0.003$ are also added to help visualize the axial waves. The system is shown rotated by 90° in the counterclockwise direction.

axial locations and begin to move upwards, i.e. leftwards in the rotated figure. This motion becomes apparent by comparing the positions of the inflows between the first ($t = 0$) and second ($t = 475$) panels. The inflows of the second and fifth DW have notably moved towards the top of the system by $t = 475$ and differ from the others in that they are tilted slightly upwards (a distinctive feature of the DW which are moving upwards). The inflows of the other DW on the other hand remain at their axial positions and only exhibit small oscillations caused by the instability discussed in the section above. As the cores of the DW travelling upwards approach the cores of the adjacent DW, they experience an attractive interaction which results in the first and fourth DW (indicated by red rightwards arrows) travelling axially downwards, i.e. rightwards in the rotated figure. Note that, as opposed to the DW moving upwards, the inflows of the DW moving downwards are tilted downwards. The attractive interaction between DW becomes stronger as their cores get close to each other, leading to a rapid increase of their travelling speeds. This characteristic results in the typical parabolic shape exhibited by the merging events in the space–time plot shown in figure 1. Another feature that is clearly illustrated in figure 11 is the increase in the tilting angle of the inflows as the DW approach one another. This angle is initially very small (see e.g. panel for $t = 730$) but increases rapidly as the mutual interaction between DW becomes stronger, reaching a value of approximately 30° with respect to the radial axis by the time when the merging of the DW takes place (see panel for $t = 836$).

After the merging events are completed, a flow pattern characterized by four DW emerges (see panel for $t = 865$), which retains a discrete translational symmetry along the z -direction (i.e. the flow pattern remains invariant if it is shifted by 2π in the axial direction). As can be seen from figure 1(c), this flow pattern undergoes subsequent merging events, which occur again simultaneously, when t is between 865 and 2320. After this second pair of merging events, the axial symmetry of the flow is fully broken (not shown) and the dynamics of the distinct DW is fully decoupled. It is only after the latter happens that the sequence of merging and splitting events begins and the number of DW in the system may either grow or decay. This initial cascade of merging events leading to a complete symmetry breaking is always observed in the simulations at the beginning of the VMS regime and can thus be interpreted as a transitional stage where the coupling between DW is fully broken. It must be finally noted that the time scale associated with merging events is highly variable and depends crucially on the distance between the cores

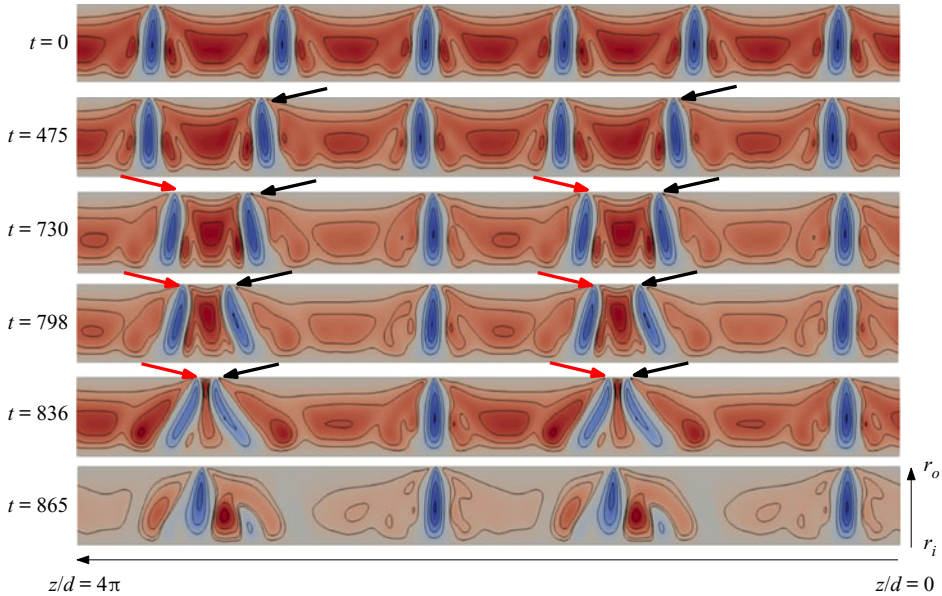


Figure 11. Colour maps of u illustrating the simultaneous occurrence of two merging events at the beginning of the VMS regime. They correspond to a simulation performed at constant $El = 0.32$, whose space–time diagram was shown in figure 1(c). The dashed (green) rectangle in the latter figure indicates the time window that is illustrated in the current figure. Positive (negative) values of u are shown as red (blue), whereas $u = 0$ is shown as grey. In each panel there are four positive and four negative contours evenly distributed in $u \in [-0.071, 0.013]$. The system is shown rotated by 90° in the counterclockwise direction.

of the two DW undergoing the merging event. They may occur very slowly, extending over nearly 1000 advective time units, such as the merging process exemplified in figure 11, or very quickly, within 50 to 100 advective time units, like the ones discussed in the next paragraph.

A central aspect of the dynamics in the VMS regime is the emergence of transient chaotic motion interspersed between merging and splitting events. As seen in figure 1, this chaotic dynamics appears localized in the vicinity of the region where a merging event has taken place and it is characterized by the repeated emergence of closely spaced, weak vortices which merge shortly after they form, creating a quick succession of merging and splitting events. The characteristic cycle of this transient dynamics is exemplified in figure 12, which shows the evolution of the flow pattern in a narrow temporal window of the simulation performed at $El = 0.32$ (see the solid line brown rectangle in figure 1c). In this example, the chaotic dynamics occurs in the central part of the system, framed by a dashed (orange) rectangle in the figure, and has little effect on the DW located outside this region. When a merging event is accomplished (see upper panel), the energy released by the DW which is eliminated is transferred to an irregular wavy motion. This wave transports the energy axially upwards and downwards from the location where the merging took place and results in the formation of new vortices (the inflows of the newly created vortex pairs are indicated with arrows in the intermediate panel). The amount of time it takes from the end of the merging event until the new vortices are fully formed normally ranges between 20 and 30 advective time units. The new vortices are, however, just a small distance apart from each other, so that they undergo a strong attractive interaction and quickly merge (see lower panel). The energy released after the new merging events is again redistributed and the process just described starts over again.

Vortex merging and splitting events in viscoelastic TCF

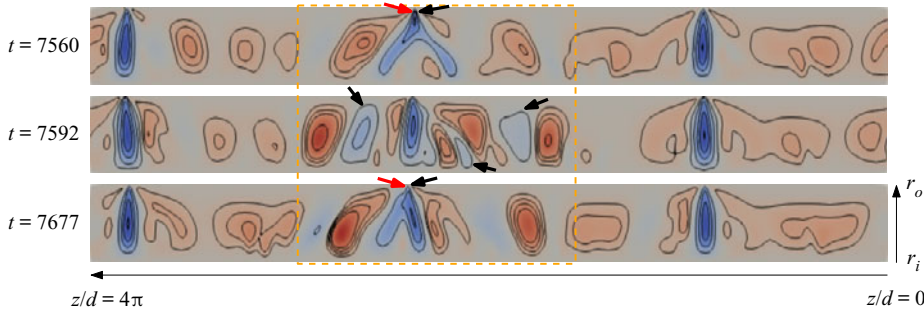


Figure 12. Colour maps of u illustrating the flow patterns associated with the chaotic dynamics that appears interspersed between slow merging events and splitting events. The dynamics displayed in this figure corresponds to the simulation with constant $El = 0.32$, and more specifically, to the time window shown as a solid line (brown) rectangle in figure 1(c). Positive (negative) values of u are shown as red (blue), whereas $u = 0$ is shown as grey. There are four positive and four negative contours evenly distributed in $u \in [-0.073, 0.013]$. The system is shown rotated by 90° in the counterclockwise direction.

The time span between consecutive merging events is of the order of 100 advective time units, whereas the entire time period over which the chaotic dynamics typically extends ranges from 1000 to 2000 advective time units.

The main splitting events (i.e. events where a new, strong and persistent DW is created) are normally preceded by chaotic motion and take place when the distance between newly created DW, as well as the distance between these and the other DW in the system, become sufficiently large so that their mutual interaction is weak. An example of a splitting event taking place between $t = 5300$ and $t = 5470$ in the simulation performed at $El = 0.32$ (see the dash-dotted purple rectangle in figure 1(c)) is shown in figure 13. The splitting event occurs in the region marked by the (red) dotted rectangle. The DW that appears within this region in the upper panel of the figure (indicated by a leftwards arrow) is the result of a merging event which has just completed. The other two DW in the figure (which are enclosed in a green dashed rectangle) are moving towards each other as a part of a merging process that will be completed after the splitting event takes place. Hence, the distance between the core of the topmost DW and those of the other two DW becomes increasingly large with time. This enables that when a new DW appears in the space left between them (see intermediate panel, where the new DW is indicated by a rightwards arrow), it can be sufficiently far apart from its neighbours to avoid a strong attractive interaction. As a result, the new DW does not undergo any merging events shortly (in contrast to what happens during the transient chaotic motion) and its strength increases until it becomes comparable to that of the other DW in the system (see lower panel). The new DW is connected to the topmost DW through the outflows, which is an indication that these DW will eventually undergo a merging event. However, such event happens at $t \sim 5930$ (see figure 1(c)), nearly 500 advective time units after the new DW first appeared. In general, the DW created after primary splitting events are found to persist for several hundred advective time units, as opposed to the vortices created during the chaotic dynamics which never persist longer than a few tens of advective time units.

The dynamics illustrated by these examples repeats successively with time, creating a chaotic regime characterized by continuous changes in the number of DW (the regime that has been dubbed VMS regime). Power spectral characterization of this flow regime is shown in figure 14. The spectra were computed by applying a fast Fourier transform to time series of the radial velocity at the mid-gap obtained from simulations where El was

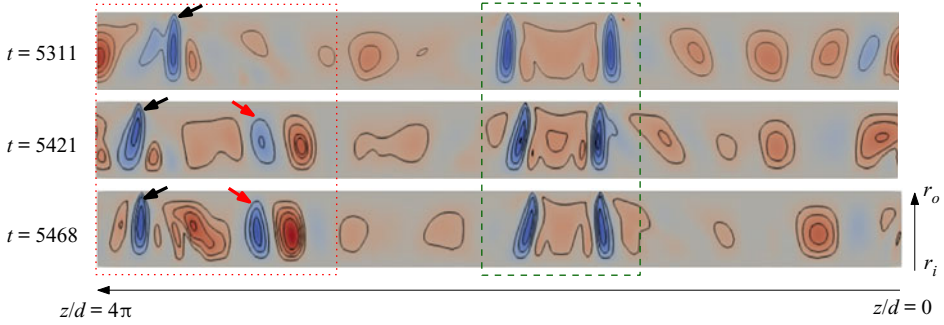


Figure 13. Colour maps of u illustrating the occurrence of a splitting event. The example shown corresponds to the simulation with constant $El = 0.32$ and it is indicated as a dash-dotted (purple) rectangle in figure 1(c). Positive (negative) values of u are shown as red (blue), whereas $u = 0$ is shown as grey. There are four positive and four negative contours evenly distributed in $u \in [-0.077, 0.015]$. The system is shown rotated by 90° in the counterclockwise direction.

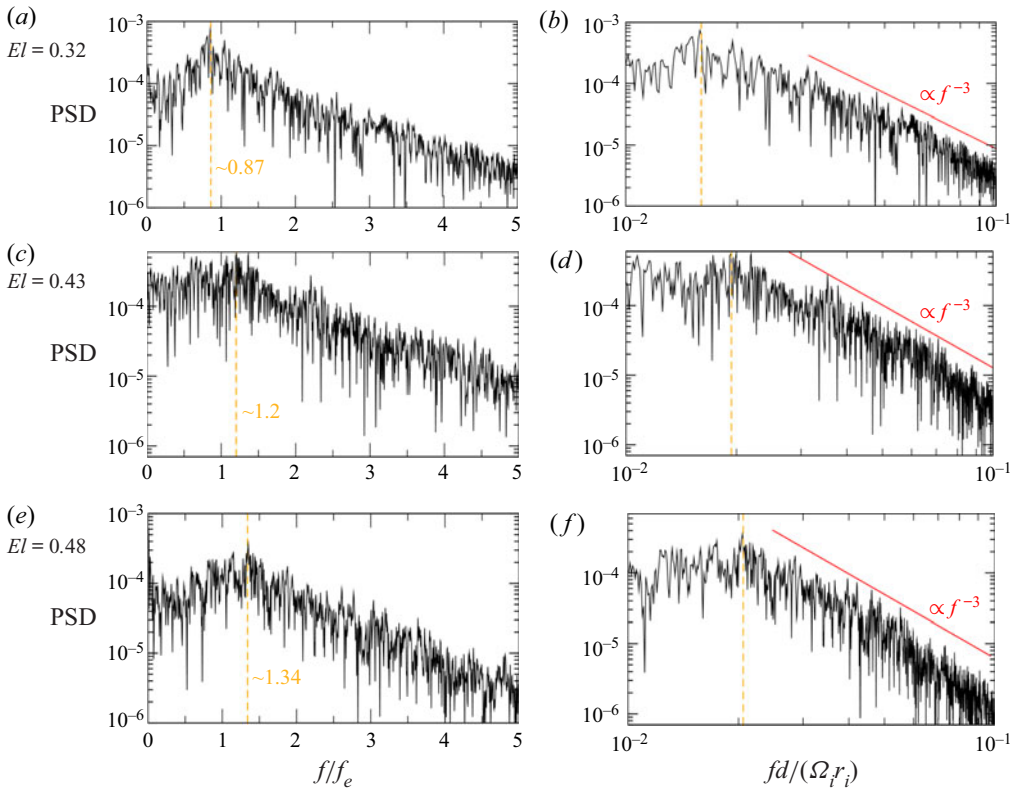


Figure 14. PSD obtained from simulations in the VMS regime at three distinct values of El . The left panels show the spectra in a linear–log plot, with the frequency normalized with the elastic frequency, f_e , whereas the right panels show the spectra in log–log scale and the frequency is non-dimensionalized with the inverse of the advective time.

held constant. The PSD increases at the lowest frequencies until it reaches a maximum (indicated as a dashed orange line in the figure). For the range of El values investigated, the frequency at which the maximum takes place is close to f_e and increases with increasing El , from $0.87f_e$ at $El = 0.32$ to $1.36f_e$ at $El = 0.5$. After the peak, the PSD decreases monotonically and exhibits to a good approximation a power law decay range with a decay rate of -3 (the best fit to the data yields exponents ranging between -2.82 and -3.33). This exponent is in agreement with the universal spectral decay rate that was theoretically predicted for EIT (Fouxon & Lebedev 2003), which has been recently verified in experiments (Yamani *et al.* 2021), and thereby identifies the VMS regime as a class of elasto-inertial turbulent states. It must also be remarked that the power spectra obtained at different El values are similar. This observation suggests that flows in the VMS regime are not significantly affected by changes in El .

3.5. Influence of the domain size and other computational parameters

Since VMS events arise from interactions among DW, it is natural to wonder about the impact that changes in the length-to-gap aspect ratio Γ (and consequently in the number of DW the system may contain) may have on the findings reported in the previous subsections. To investigate this aspect, a set of simulations where Γ was varied between 9 and 16 has been conducted. The protocol followed in these simulations is the same as that described at the beginning of § 3.1: they are started from a Newtonian TVF and El is slowly increased with time at a uniform rate, $El = 10^{-3}t/Re$, where Re was again fixed to 95. The influence of the initial condition has also been examined. To this end, two or three simulations have been performed for each value of Γ considered and these have been started from states having a different number of vortex pairs. A complex spatio-temporal dynamics consistent with the VMS regime has been observed in all cases. However, the El threshold at which merging events first appear changes significantly depending on the domain size and the initial condition. This is illustrated in figure 15, which shows space–time diagrams of u at the mid-gap along the z direction for simulations where (a) $\Gamma = 10$ and the initial condition has five vortex pairs, (b) $\Gamma = 14$ and the initial condition has eight vortex pairs and (c) $\Gamma = 14$ and the initial condition has six vortex pairs. Note that, analogously to figure 1(a), time has been replaced by its corresponding El value. As seen, the first merging events are accomplished at notably different values of El in each case: $El \approx 0.16$ in (a), $El \approx 0.21$ in (b) and $El \approx 0.28$ in (c), which in turn differ from the onset of merging events reported in § 3.1 ($El \approx 0.32$ for $\Gamma = 12.56$, using a state with six vortex pairs as initial condition). It is therefore evident that this feature is very sensitive to the domain size and the initial condition used in the simulations. The same is true for the onset of chaotic motion. For the Γ values and initial conditions investigated, the first occurrence of a merging event has been found to range between $El \approx 0.15$ and $El \approx 0.32$, whereas chaotic motion has been first observed at El values ranging from 0.25 to 0.42.

The characteristics of the transition towards the VMS regime are not significantly altered by changes in Γ or the initial condition. As El increases initially from the Newtonian limit, a centrifugally dominated regime is identified in all cases, where the axial extent of the inflows (outflows) gradually decreases (increases) with increasing El . This behaviour continues until the elastic instability sets in abruptly and the intensity of the inflows becomes much higher. This can be seen in figure 15 as a sudden change in the colour intensity that happens at $El \approx 0.125$. It is interesting to note that, despite the significant variation in the El values at which the VMS events occur, the threshold of the elastic

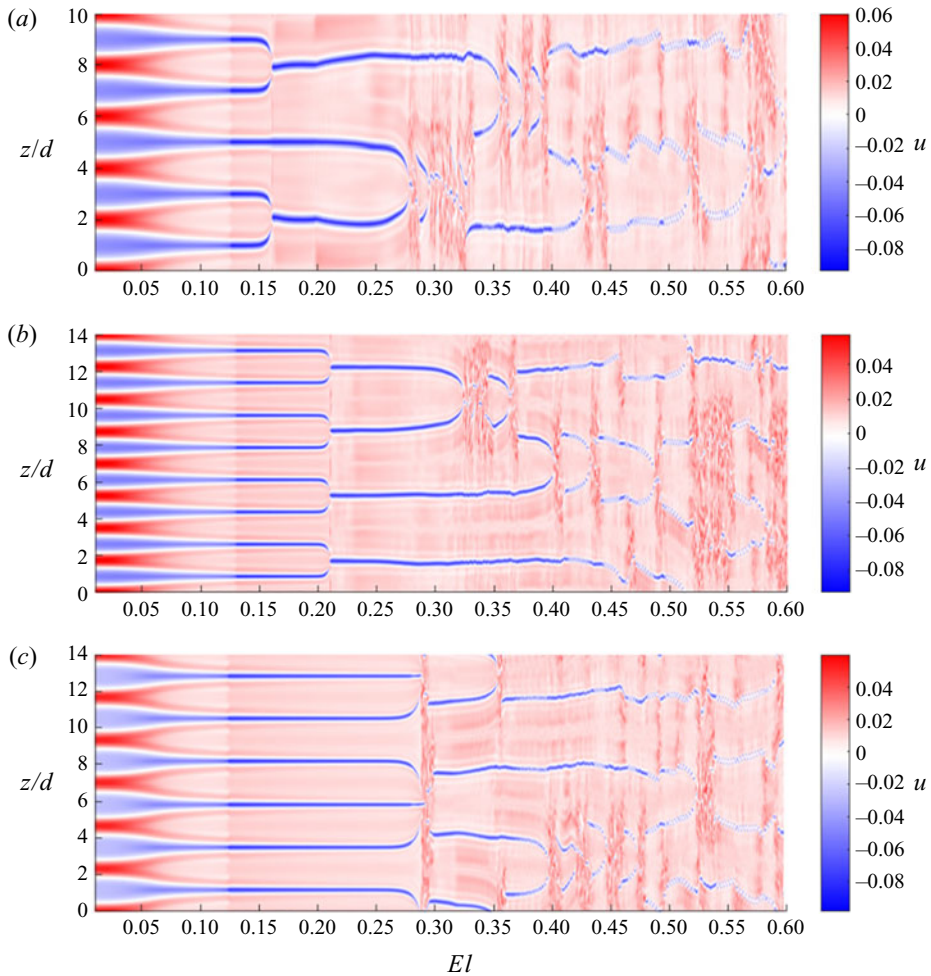


Figure 15. Space–time diagrams showing the magnitude of u at the mid-gap along the z direction in simulations where the axial length of the system and/or the number of vortex pairs of the initial condition were varied with respect to the simulations shown in figure 1. The cases illustrated correspond to (a) $\Gamma = 10$ using an initial condition with five vortex pairs, (b) $\Gamma = 14$ using an initial condition with eight vortex pairs and (c) $\Gamma = 14$ using an initial condition with six vortex pairs. As in the simulations presented in figure 1, El has been slowly increased with time ($El = 10^{-3}t/Re$) and the latter has been replaced by its corresponding El value in the horizontal axis of the space–time plots. Red and blue areas indicate outflows and inflows respectively. Note that periodic boundary conditions are used in z .

instability remains nearly unchanged with varying Γ or initial condition (it is always found to occur at El values ranging from 0.12 to 0.13). Another feature that is shared by all simulations regardless of the domain size and initial condition is the existence of an initial stage of merging events, with some of them taking place simultaneously, that precede the appearance of chaotic motion. A previously unreported event, where three DW merge simultaneously, has been observed in some simulations within this initial stage (see figure 15c). This particular type of merging event occurs when there is a group of three equal DW in which the upper and lower DW move towards the central DW. The forces exerted by the upper and lower DW on the central DW are equal and act in opposite senses, so that the central DW does not move and eventually the three DW

Vortex merging and splitting events in viscoelastic TCF

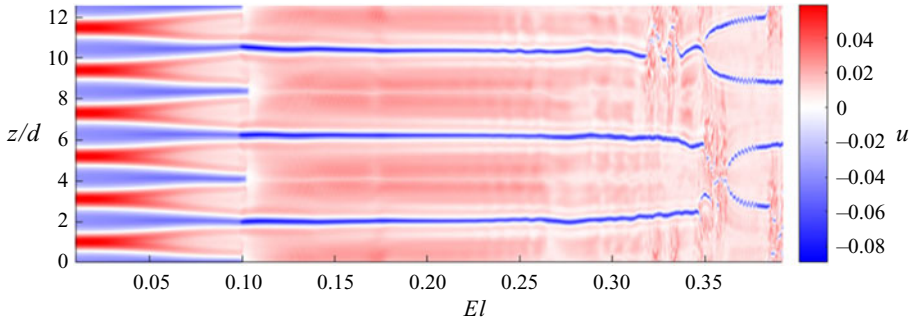


Figure 16. Space–time diagram showing the magnitude of u at the mid-gap along the z direction in a simulation where El was slowly decreased with time at the same rate as it was increased in the simulations previously presented ($El = 10^{-3}t/Re$). The parameters used in this simulation are the same as those used in the simulation shown in § 3.1. The initial condition corresponds to the state obtained in the simulation where El was slowly increased with time for $El = 0.392$ (indicated by an orange dashed line in figure 1a). The flow states observed when El decreases differ from those obtained when El increases, evidencing the existence of hysteresis. Red and blue areas indicate outflows and inflows, respectively. Note that periodic boundary conditions are used in z .

merge simultaneously. The main difference between the transition scenarios illustrated in figure 15 and that described in the previous subsections is the absence of the regime characterized by the small axial oscillations of the flow pattern. This regime preceded the onset of the VMS regime in the simulation for $\Gamma = 12.56$. The same axial oscillations are observed in figure 15 at large El values. However, merging and splitting events occur prior to the emergence of the oscillations in these cases. This clearly indicates that the occurrence of these oscillations is not a necessary condition for the VMS dynamics to exist, but an additional dynamics that occurs at large El values and may or not coexist with the VMS events.

The strong dependence of the onset of the VMS events on the initial condition implies that these are highly nonlinear phenomena. It is thus rational to expect that hysteretic behaviour will be observed in the simulations if the control parameter is varied in the reverse direction, i.e. if El is decreased with time. To examine this possibility, we have conducted a simulation where El has been decreased with time at the same rate as it was increased in the previous simulations. The simulation was initiated from the flow state obtained at $El = 0.392$ in the simulation presented in § 3.1 (indicated by a dashed line in figure 1a) and the same parameter values as in § 3.1 were used. To facilitate the description, we denote the simulation in which El increases (decreases) with time as forwards (backwards) simulation. Figure 16 shows the space–time diagram corresponding to the backwards simulation. It becomes apparent from the comparison between this figure and the space–time diagram of the forwards simulation (figure 1a,b) that there is a strong hysteresis. The flow in the backwards simulation eventually returns to the initial state of the forwards simulation (a TVF with six pairs of vortices), but it follows a completely different path, characterized by VMS events and flow states that differ from those observed in the forwards simulation. It is worth noting that the initial cascade of merging events that precede the onset of chaotic motion in forwards simulations is absent in the backwards simulation. This reflects the irreversible character of the symmetry-breaking processes that take place over this initial stage of the VMS regime. Another notable difference is observed in the transition between the centrifugally and elastically dominated regimes. This occurs at a lower El value ($El \approx 0.09$) than in the forwards simulations ($El \approx 0.125$)

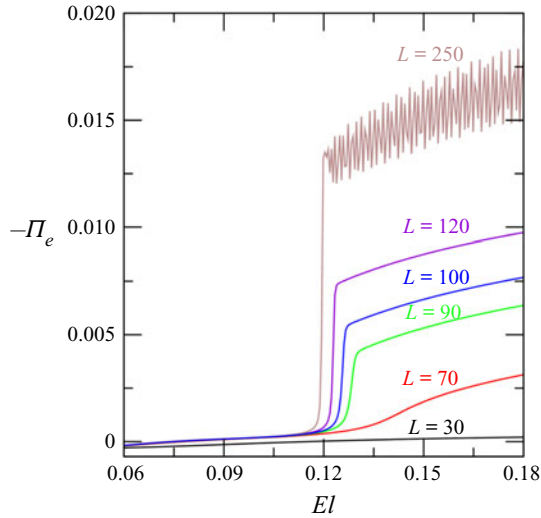


Figure 17. Contribution of the elastic stresses to the integral kinetic energy budget Π_e as a function of the maximum polymer extension L in the range of El values where the transition between the centrifugally and elastically dominated regimes takes place.

and not only entails a sudden change in the strength of the vortices, but also a change in their number (from three vortex pairs in the elastically dominated regime to six vortex pairs in the centrifugally dominated regime). Once the centrifugally dominated regime is achieved, flow states obtained in the forwards and backwards simulations for the same El values become identical. This observation reflects the linear nature of the centrifugal instability and evidence that the hysteretic effects observed in the simulations are solely due to the subcritical character of the DW.

We next examine whether the occurrence of VMS events depends on the extensibility of the polymers used in the simulations. To this end, we have conducted a set of simulations where the maximum polymer extension L was varied between 30 and 250 while keeping the other parameters as in § 3.1. It has been found that the choice of L has an important impact on the characteristics of the elastic instability. This is illustrated in figure 17, which shows the contribution of the polymers to the integral energy budget (Π_e) in the range of El values where the elastic instability takes place. As shown earlier in figure 6, the onset of the elastic instability leads to a marked increase in the value of Π_e , which replaces the energy production due to inertia (\mathcal{P}) as the leading term that balances the viscous dissipation (ϵ). This characteristic is absent in simulations where the extensibility of the polymers is low (see $L = 30$ case in the figure). In these simulations, Π_e increases very gradually with increasing El and remains negligible with respect to \mathcal{P} and ϵ for the entire range of El investigated (up to $El = 0.5$). This implies that at these elasticity levels the elastic instability does not occur in these cases. As a result, the VMS dynamics does not take place and the flow at high El values is characterized by elastically modified Taylor vortices (not shown). A clear increase in Π_e consistent with the emergence of an elastic instability is observed in the simulations when these are performed using $L \gtrsim 70$. The El threshold at which the instability sets in decreases slightly with increasing L (from $El \approx 0.135$ for $L = 70$ to $El \approx 0.115$ for $L = 250$). The transition between the centrifugally and elasticity dominated regimes is initially rather smooth (see $L = 70$ case) but it becomes increasingly sharp as L increases. As the transition gets sharper

Vortex merging and splitting events in viscoelastic TCF

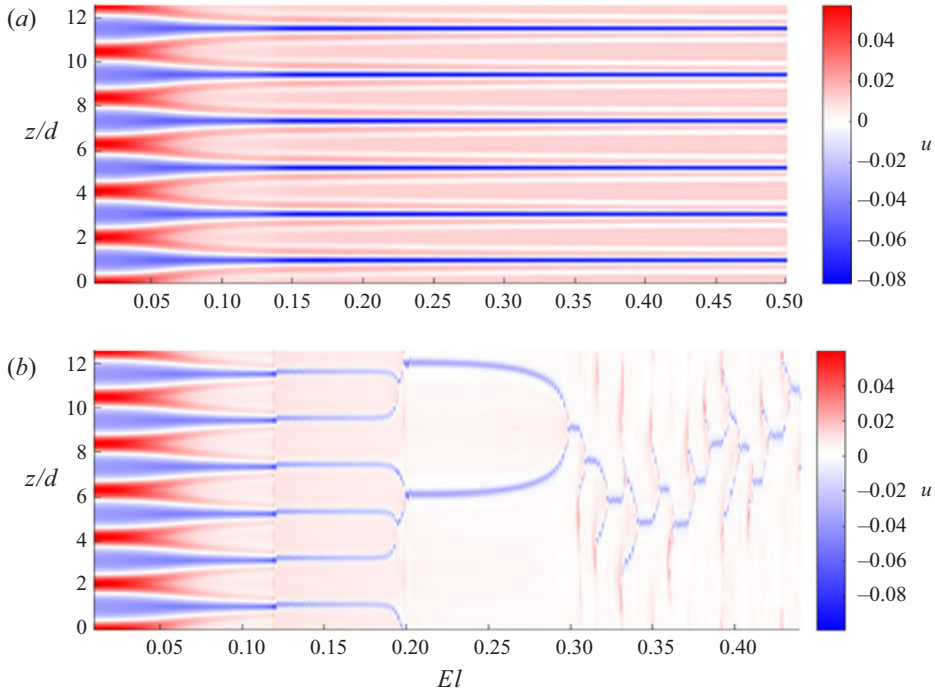


Figure 18. Space–time diagram showing the magnitude of u at the mid-gap along the z direction in simulations where the maximum polymer extension was set to $L = 70$ (a) and $L = 250$ (b). The rest of the parameters were kept as in § 3.1. Red and blue areas indicate outflows and inflows, respectively.

the magnitude of Π_e increases substantially, leading to increasingly strong vortices and causing the emergence of spatio-temporal dynamics right after the transition in cases where very large extensibility is considered (see $L = 250$ case, where oscillations in the value of Π_e arise simultaneously with the transition).

The onset of the VMS dynamics (which has been observed in the simulations where $L \geq 90$) also takes place at smaller values of El as L increases. It is interesting that, although the elastic instability is observed for $L = 70$, the space–time diagram of this simulation (shown in figure 18a) does not show any sign of spatio-temporal complexity. This might reflect that the emergence of VMS events requires elasticity levels higher than those simulated here when L is close to the critical value for which the elastic instability emerges. The most striking difference in the characteristics of the VMS regime with respect to those observed in the previous simulations occurs when highly extensible polymers are used. Here, after the initial cascade of merging events is accomplished, the dynamics is characterized by a sequence of VMS events that exhibits a clear periodicity (see figure 18(b), which shows the space–time diagram for the simulation using $L = 250$). These structures are closely reminiscent of the flame-like patterns observed in previous studies (Thomas *et al.* 2006, 2009; Liu & Khomami 2013), with the difference that, in these studies, the flow was non-axisymmetric and the flame-like dynamics was superposed with a rotating wave, whereas in the present study the flow is axisymmetric and therefore the rotating wave is absent.

We have finally investigated the effect of varying the rate at which El is increased in the simulations. The increase of the El value with time ($El = \alpha t/Re$) can be understood

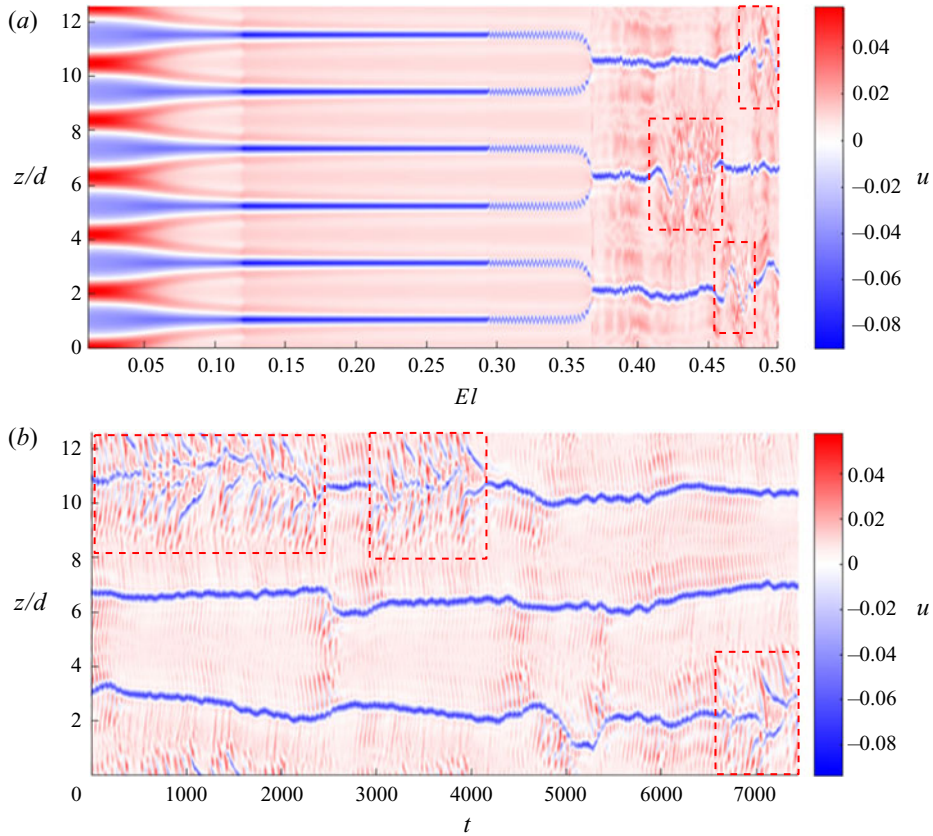


Figure 19. Example of the dynamics observed in the simulations when α (i.e. the rate of increase in El) is larger than 1.25×10^{-3} . (a) Space–time diagram showing the magnitude of u at the mid-gap along the z direction in a simulation where $\alpha = 1.6 \times 10^{-3}$. The rest of the parameters are as in § 3.1. (b) Space–time plot obtained when El is held constant at 0.5 in the simulation shown in (a). The dashed (red) rectangles demarcate regions of transient chaotic dynamics. Red and blue areas indicate outflows and inflows, respectively.

as a continuous perturbation that is imposed on the system, where the parameter α (the rate of increase) regulates the amplitude of the perturbation. We have conducted simulations varying α between 7.5×10^{-4} and 5×10^{-3} , while keeping the other parameters as in § 3.1. The VMS regime (with characteristics similar to those reported in the previous subsections) was found in the simulations where $7.5 \times 10^{-4} \lesssim \alpha \lesssim 1.25 \times 10^{-3}$. However, when α was set to higher values, the VMS dynamics did not occur. Panel (a) of figure 19 illustrates the space–time plot as a function of El for a simulation where $\alpha = 1.6 \times 10^{-3}$. As seen, the variation of the vortex pattern with increasing El is initially analogous to that observed when $\alpha = 1 \times 10^{-3}$ (figure 1a). The transition between the centrifugally and elasticity dominated regimes taking place at $El \approx 0.12$ is clearly identified by the sudden change of the colour intensity of the vortices. Also as in the simulation for $\alpha = 1 \times 10^{-3}$, the vortex pattern becomes unstable at $El \approx 0.29$, resulting in small axial oscillations of the DW. These oscillations persist until several merging events take place simultaneously and break the axial symmetry of the flow pattern (which occurs at $El \approx 0.36$). However, the flow regime that emerges after the symmetry-breaking process differs from the VMS regime. The DW remain at approximately the same axial

Vortex merging and splitting events in viscoelastic TCF

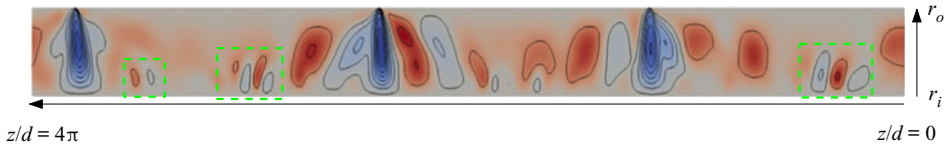


Figure 20. Colour map of u illustrating the instantaneous flow structure at $El = 0.5$ in a simulation where $\alpha = 5 \times 10^{-3}$. Positive (negative) values of u are shown as red (blue), whereas $u = 0$ is shown as grey. There are 10 contours evenly distributed in $u \in [-0.065, 0.015]$. The system is shown rotated by 90° in the counterclockwise direction. Dashed (green) rectangles are used to highlight the small scale vortices that emerge near the inner cylinder.

positions and their number does not change with increasing El , nor with time if El is held constant, as shown in panel (b) of the same figure. Similar to the VMS regime, localized transient chaotic dynamics is often observed in this flow regime (see regions enclosed by the dashed red rectangles). As shown in figure 20, a particular feature of the flow structure in this flow regime is the emergence of small scale vortices near the inner cylinder (see regions demarcated by the dashed green rectangles). These vortices are consistent with the elastic Görtler vortices identified by Song *et al.* (2019) at higher Reynolds numbers. The finding of a flow regime distinct from the VMS regime in these simulations reflects a well-known feature of viscoelastic TCF: the coexistence of various flow regimes for the same values of the control parameters. The simulations may converge to one regime or the other depending on the amplitude and type of the perturbations imposed. Our study shows that, to capture the VMS in the simulations, the amplitude of the perturbation cannot be too large, otherwise the VMS regime is replaced by the flow regime just described.

3.6. Variation of the angular momentum transport with increasing fluid elasticity level

An important question raised by the observations above is why the dynamics of the distinct vortex pairs decouples when the polymer elasticity exceeds a certain threshold. It is well known that in two-dimensional vortex systems the conservation of angular momentum imposes strong restrictions on the motion of the vortices and the mean separation among them remains generally nearly constant (Aref 1983; Batchelor 2000). It may therefore appear surprising that vortex pairs in the VMS regime can freely move through the system, either toward each other or away from each other, without drastic changes in the system's energy. To explain this seeming inconsistency, it is instructive to examine the impact of increasing El in the different contributions to the flux of angular momentum (J^ω) across the annular gap. In a viscoelastic fluid flow, J^ω can be split into three terms

$$J^\omega = r^3 \left[\underbrace{\overline{u\bar{\omega}}}_{J_c^\omega} - \underbrace{\frac{\beta}{Re} \partial_r \bar{\omega}}_{J_d^\omega} - \underbrace{\frac{(1-\beta) \overline{T_{r\theta}}}{Re r}}_{J_p^\omega} \right], \quad (3.5)$$

where $\omega = v/r$ is the angular velocity and the bar symbol indicates averaging over the axial direction (for El values where the flow is steady) or over the axial direction and time (when the flow is non-steady or chaotic). Here, J_c^ω denotes the convective transport of angular momentum, which is associated with the vortices, J_d^ω is the diffusive transport due to viscosity and J_p^ω is the angular momentum transport caused by polymer stresses.

Although the above equation was originally derived for turbulent flow (Eckhardt, Grossmann & Lohse 2007; Song *et al.* 2019), it is straightforward to show that it also

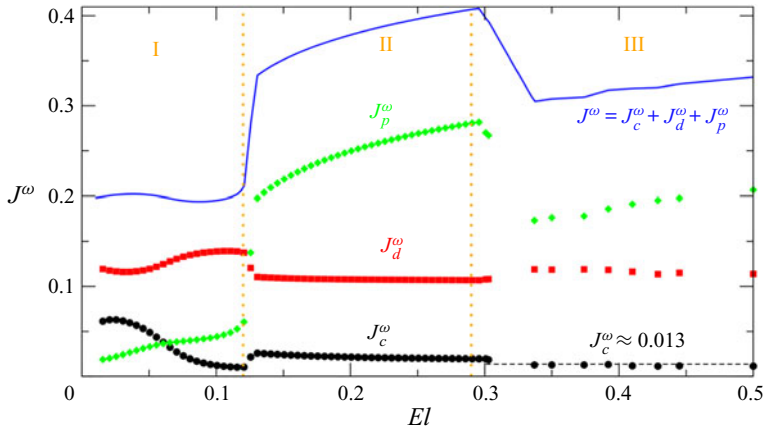


Figure 21. Variation of the axially and time averaged angular momentum current (J^ω) and its contributing terms, J_c^ω , J_d^ω and J_p^ω , obtained near mid-gap, as El increases. The (orange) vertical dotted lines demarcate the different flow regimes observed in the present study: I. the centrifugally dominated regime, II. the elastically dominated regime characterized by steady patterns of equally spaced DW, III. the elastically dominated regime characterized by spatio-temporal dynamics.

applies to steady vortex flow (see [Appendix B](#) for a step by step derivation under steady and axisymmetric conditions). Hence, it can be used to study the variation in the contributions of the different transport mechanisms as El increases from the Newtonian limit up to the largest value simulated within the VMS regime. This is shown in [figure 21](#) for a radial location near the mid-gap using the data obtained from the simulation presented in [§ 3.1](#) (similar analyses for other simulations are shown in [Appendix C](#)). Since the dynamics in the VMS regime is chaotic and J^ω is a fluctuating quantity, several additional simulations at constant El had to be performed in order to obtain meaningful values of J^ω and its contributing terms in this flow regime. The initial conditions for these simulations were flow states obtained in the simulation with slowly varying El . Starting from these solutions, the El values were fixed and the chaotic flow was simulated in each case for 20000 advective time units. The momentum fluxes were then calculated by averaging over this long time period.

As seen in the figure, three clear stages can be distinguished in the behaviour of the angular momentum fluxes as El increases, which are consistent with the different flow regimes identified throughout our study. In the first stage, coinciding with the centrifugally dominated regime, J^ω remains nearly constant. While its main contribution stems from the diffusive transport (J_d^ω), the convective flux (J_c^ω) also plays an important role close to the Newtonian limit ($El \rightarrow 0$). However, due to the dissipative nature of the polymer activity in this flow regime, the contribution of the vortices to J^ω decays with increasing El and it is gradually replaced by the angular momentum flux due to the polymer stresses (J_p^ω). Note that, although it may seem surprising that the contribution of J_d^ω exceeds that of J_c^ω in a Newtonian (or low El) vortex flow, this happens because the simulation is conducted at a Reynolds number ($Re = 95$) which is very close to the onset of the Taylor vortices ($Re = 89$). Here, the vortices are still weak and the momentum transport is dominated by molecular diffusion (as in the laminar regime). As Re increases, the contribution of J_c^ω near the mid-gap becomes increasingly large and the contribution of J_d^ω decreases, so that the former eventually dominates the momentum transport in this regime (not shown). The onset of the elasticity dominated regime ($El \sim 0.12$) is accompanied by an abrupt increase

in J_p^ω , which becomes the leading contribution to the angular momentum flux. Moreover, the magnitude of J_p^ω keeps increasing as El increases, leading to a substantial increase in J^ω with respect to that in the centrifugally dominated regime. The convective and diffusive fluxes, on the other hand, exhibit a slight increase and decrease, respectively, when the elastic instability sets in, and subsequently decrease very gradually with increasing El . The onset of the spatio-temporal dynamics ($El \sim 0.29$) brings a significant drop in the total angular momentum flux. This is mainly associated with an initial decay in J_p^ω that takes place during the initial cascade of merging events where the different vortex pairs become fully decoupled. Despite its initial decrease, J_p^ω is still the main contribution to J^ω , and after the initial phase of merging events, its magnitude increases with increasing El over the entire VMS regime. The convective contribution J_c^ω also decays during the initial phase of merging events. However, it appears to fluctuate around a constant value, $J_c^\omega \approx 0.013$, with increasing El . A similar behaviour is observed in J_d^ω , which increases initially with the emergence of the VMS dynamics but remains subsequently nearly constant as El increases.

The analysis of the angular momentum fluxes just presented allows us to propose an answer to the question posed at the beginning of this section. As shown, polymer stresses are very efficient in transporting angular momentum (provided that the level of elasticity in the working fluid is sufficiently large) and so the contribution of the vortices in this regard, which is essential in the Newtonian case, is only marginal in the viscoelastic case. The amount of momentum carried by the vortices becomes increasingly small as El increases until it eventually reaches a nearly constant level, $J_c^\omega \approx 0.013$, in all simulations where the VMS is found. On the basis of this observation, we suggest that, when the angular momentum carried by the vortices drops to this level, the constraints imposed by the angular momentum conservation on the vortices break and these may decouple from the rest of the system. This limit would mark the beginning of the VMS dynamics and could also be interpreted as the minimum amount of angular momentum that the DW must carry to form a pattern of steady vortices. The latter interpretation offers an explanation for the question of why the DW do not merge at lower El values. As noted in § 3.1, arrangements of equally spaced, steady DW have not been so far experimentally reported. In fact, it has been inferred from the experiments that two DW coalesce when the distance between them is lower than $5d$, a characteristic that would render the formation of these arrangements of DW unfeasible. The reason for this apparent contradiction may lie in the fact that these experiments were conducted at low values of Re , where the flow in the Newtonian case is centrifugally stable (i.e. molecular diffusion suffices to transport angular momentum). The amount of angular momentum carried by the DW at these low Re is expected to be very small and hence it is reasonable to assume that it might be below the threshold required to observe these arrangements. Another important remark concerning the angular momentum fluxes in the VMS regime is that the two Newtonian contributions (J_c^ω and J_d^ω) remain nearly constant over the entire regime. The increase in the angular momentum flux taking place in this flow regime is thus only due to the contribution of the polymer stresses, which continue increasing with increasing El . This circumstance strongly suggests that the dynamics in the VMS regime is fully dominated by elastic effects (as already noted in the experimental study by Lacassagne *et al.* 2020) and raises the question about a possible relationship between flow states in the VMS regime and those driven by pure elastic instabilities in the inertialess limit.

4. Conclusions

We have presented numerical simulations of viscoelastic TCF aimed at elucidating recent experimental observations of an elastically induced chaotic dynamics governed by a successive merging and splitting of vortices, known as the VMS transition to EIT (Lacassagne *et al.* 2020). Unlike the experiments, where this regime was achieved by increasing Re while keeping a constant El level, in the present study we have fixed Re to 95 (a value that falls within the centrifugally unstable regime of TCF) and have increased El progressively starting from a TVF pattern in the Newtonian limit ($El = 0$). This different protocol has allowed us to investigate the transformation and instabilities that the axisymmetric vortex flow pattern undergoes as El increases and the VMS regime is achieved.

Our simulations show that, unlike other transition scenarios to elasto-inertial turbulent states (e.g. the transition via flame patterns (Latrache & Mutabazi 2021) or the transition driven by defects Latrache *et al.* 2016), the transition to the VMS regime does not involve any three-dimensional instability and it is associated with instabilities of an axisymmetric vortex pattern which are induced solely by elastic effects. The centrifugal instability mechanism giving rise to the well-known Taylor vortices is found to persist at low-to-moderate values of El . Nevertheless, polymers induce strong dissipative effects in this flow regime, causing drastic quantitative and structural changes in the vortex pattern. These changes are particularly pronounced at low El values, thereby evidencing the immediate and dramatic impact that the addition of polymers has on the flow characteristics.

A key factor to explain the complex spatio-temporal dynamics observed at high El values is the transformation the flow undergoes at $El \approx 0.12$. Above this El threshold, polymers inject energy into the flow through the elastic stresses and the centrifugal mechanism inducing the vortex pattern is replaced by an elastic mechanism. The result of the elastic instability is a steady vortex pattern where the vortex pairs are identified as DW: a type of vortical structure similar to a dipole which is characterized by a strong asymmetry between inflows and outflows. While these structures have been well documented in the literature (Groisman & Steinberg 1997; Lange & Eckhardt 2001; Thomas *et al.* 2006, 2009), there are some important differences between the state found in our simulations and those previously reported. The first important distinction is the pathway we have followed to find these structures. Previous experiments and simulations suggested that DW could only emerge as the inner cylinder speed is decreased (i.e. as Re decreases). In our simulations, however, DW appear at a constant value of Re as El increases, reflecting that deceleration is not a necessary condition to observe these structures. A second and more important distinction is the spatial arrangement of the DW. Previous studies on DW were conducted at low Re values (in centrifugally stable regimes) where it was found that nearby DW always approach each other and coalesce into a single entity. As a result, after a certain time DW usually appear as solitons in these flow regimes. Our simulations reveal that, in a centrifugally unstable regime, DW do not necessarily merge when they are close to each other, and may appear for a wide range of El values as a steady vortex pattern.

VMS events take place when the dynamics of the distinct DW decouples and these begin to travel freely in the axial direction. We propose that this dynamical decoupling is possible because as El increases the amount of angular momentum carried by the vortices reaches a marginal level (the angular momentum transport across the gap is mainly due to the polymer stresses). This circumstance permits the vortices to break the constraints that conservation of momentum imposes on their motion, thus making it possible for them to be dynamically disconnected. During the onset phase of the VMS

regime only merging events are observed, but with further increase in El , a complex spatio-temporal dynamics characterized by a series of merging and splitting events, which closely resembles experimental observations, is also found in the simulations. Merging events occur when two DW move in opposite senses towards each other. As they get close to one another, they experience a strong attractive interaction that increases their travelling speeds and accelerates the merging process. Conversely, splitting events occur when newly created vortex pairs move away from each other and get separated by a distance that is sufficiently large so that their mutual interaction is weak. The occurrence of splitting events is always preceded by local regions of transient chaotic motion which result from merging events as a consequence of the redistribution of the kinetic energy released by the DW that are eliminated in these events. A key feature of the VMS regime is the existence of a power law decay range in the power spectrum with a -3 exponent. Such a decay rate complies with the universal power law spectral decay expected for EIT (Fouxon & Lebedev 2003; Yamani *et al.* 2021) and thus suggests categorizing the VMS regime as a class of the elasto-inertial turbulent states.

Due to the highly nonlinear nature of the DW, changes in the aspect ratio and/or the number of vortex pairs of the initial condition may notably alter the El threshold at which the VMS regime sets in. Specifically, the onset of this regime has been found to vary between $El \approx 0.15$ and $El \approx 0.35$ depending on the aspect ratio and the initial condition used in the simulations. This range of El values is consistent with the elasticity level at which this dynamics has been reported in the experiments, $El \approx 0.22$ (Lacassagne *et al.* 2020). The characteristics of the VMS events, as well as the transition towards the VMS regime as El increases, are largely similar in all simulations. The main exception is the regime characterized by the small axial oscillations of the DW, i.e. the standing wave described in § 3.3. This regime precedes the VMS dynamics in simulations where the latter occurs at high El values, but it is absent in those where VMS events already occur at moderate values of El . In these latter cases, the oscillations are also observed at high El values, but they coexist with the VMS dynamics. Hence, it may be concluded that the emergence of the standing wave is not a necessary condition for the onset of the VMS regime.

We have also studied how changes in the maximum polymer extension L and the parameter α (the rate of increase in El) modify the outcomes of the simulations. It has been found that, if L is too small ($L < 70$), the elastic instability does not set in and consequently the VMS dynamics does not take place. Conversely, if L is too large ($L > 200$), the simulations converge to a different flow regime, which is consistent with the flames-like structures previously reported in the literature (Thomas *et al.* 2006, 2009; Liu & Khomami 2013). The VMS regime has been found in simulations where the value of L is between 90 and 200. An appropriate choice of α is also essential to capture the VMS in the simulations. This regime has been found in simulations where $7.5 \times 10^{-4} \lesssim \alpha \lesssim 1.25 \times 10^{-3}$. For $\alpha > 1.25 \times 10^{-3}$, however, a different flow regime emerges at high El values. VMS events do not occur in this regime (i.e. the number of vortex pairs remain constant) and small scale vortices, consistent with elastic Görtler vortices (Song *et al.* 2019), appear near the inner cylinder.

In closing, we would like to note that there are many important open questions about this topic which have not been addressed yet. For example, a detailed study of the VMS transition as Re increases, examining the changes the flow undergoes until it converges to the eventual elasto-inertial state, is missing. A statistical and structural characterization of the elasto-inertial turbulent state has not been done either, which has prevented from any comparisons with other elasto-inertial turbulent states reported in viscoelastic TCF (Liu

& Khomami 2013; Song *et al.* 2019, 2021a) or in other fluid flow systems (Dubief *et al.* 2013; Samanta *et al.* 2013). It is also unclear whether there exists a connection between this elasto-inertial turbulent regime (which requires of pure elastic instabilities to exist) and the pure elastic turbulent regime taking place at vanishing inertia. Finding answers to these and other related questions guarantees that viscoelastic TCF will be an active focus of research in the coming years.

Acknowledgements. The author thankfully acknowledges the computer resources at Pirineus and the technical support provided by the Consorci de Serveis Universitari de Catalunya (RES-IM-2022-1-0005).

Funding. This work has been supported by the grant PID2020-114043GB-I00 of the Spanish Ministry of Science and Innovation.

Declaration of interests. The authors report no conflict of interest.

Author ORCID.

 Jose M. Lopez <https://orcid.org/0000-0002-0384-2022>.

Appendix A. Energy balance equation for steady axisymmetric vortex flow

In this section it is shown that an equation for the energy associated with steady and axisymmetric vortices can be derived following a line of reasoning similar to that typically used in the derivation of the turbulent kinetic energy equation. Under conditions of steadiness and axisymmetry (i.e. $\partial_t = 0$ and $\partial_\theta = 0$), and using the notation and non-dimensionalization described in § 2, the momentum equations for a viscoelastic TCF read

$$0 = -u\partial_r u - w\partial_z u + \frac{v^2}{r} - \partial_r p + \frac{\beta}{Re} \left(\nabla^2 u - \frac{u}{r^2} \right) + \frac{1-\beta}{Re} \left(\partial_r T_{rr} + \frac{(T_{rr} - T_{\theta\theta})}{r} + \partial_z T_{rz} \right), \quad (A1)$$

$$0 = -u\partial_r v - w\partial_z v - \frac{uv}{r} + \frac{\beta}{Re} \left(\nabla^2 v - \frac{v}{r^2} \right) + \frac{1-\beta}{Re} \left(\partial_r T_{r\theta} + \frac{2T_{r\theta}}{r} + \partial_z T_{\theta z} \right), \quad (A2)$$

$$0 = -u\partial_r w - w\partial_z w - \partial_z p + \frac{\beta}{Re} \nabla^2 w + \frac{1-\beta}{Re} \left(\partial_r T_{rz} + \frac{T_{rz}}{r} + \partial_z T_{zz} \right), \quad (A3)$$

where the Laplacian term is given by

$$\nabla^2 f = \frac{1}{r} \partial_r (r \partial_r f) + \partial_z^2 f. \quad (A4)$$

We first obtain the axially averaged momentum equations. To that extent, the velocity, pressure and polymer stress tensor of the vortex flow are decomposed as

$$\mathbf{v} = \begin{bmatrix} 0 \\ \bar{v} \\ 0 \end{bmatrix} + \begin{bmatrix} u' \\ v' \\ w' \end{bmatrix}, \quad p = \bar{p} + p', \quad \mathbf{T} = \begin{bmatrix} \overline{T_{rr}} \\ \overline{T_{r\theta}} \\ \overline{T_{rz}} \\ \overline{T_{\theta\theta}} \\ \overline{T_{\theta z}} \\ \overline{T_{zz}} \end{bmatrix} + \begin{bmatrix} T'_{rr} \\ T'_{r\theta} \\ T'_{rz} \\ T'_{\theta\theta} \\ T'_{\theta z} \\ T'_{zz} \end{bmatrix}, \quad (A5a-c)$$

where the bar symbol is used to indicate that the variables are axially averaged and the prime symbol denotes deviation from the axially averaged value. Note that for a vortex

flow pattern these operators satisfy the Reynolds averaged rules (i.e. $\overline{\bar{f}'} = 0$, $\bar{f} = \bar{f}$ and $\overline{\bar{f}f'} = 0$). Substituting this decomposition into the momentum equations and averaging over the axial direction, one obtains

$$0 = -\overline{u'\partial_r u'} - \overline{w'\partial_z u'} + \frac{\bar{v}^2}{r} + \frac{\overline{v'^2}}{r} - \partial_r \bar{p} + \frac{1-\beta}{Re} \left(\partial_r \overline{T_{rr}} + \frac{\overline{T_{rr}} - \overline{T_{\theta\theta}}}{r} \right), \quad (\text{A6})$$

$$0 = -\overline{u'\partial_r v'} - \overline{w'\partial_z v'} - \frac{\overline{u'v'}}{r} + \frac{\beta}{Re} \left(\frac{1}{r} \partial_r (r \partial_r \bar{v}) - \frac{\bar{v}}{r^2} \right) + \frac{1-\beta}{Re} \left(\partial_r \overline{T_{r\theta}} + \frac{2\overline{T_{r\theta}}}{r} \right), \quad (\text{A7})$$

$$0 = -\overline{u'\partial_r w'} - \overline{w'\partial_z w'} + \frac{1-\beta}{Re} \left(\partial_r \overline{T_{rz}} + \frac{\overline{T_{rz}}}{r} \right). \quad (\text{A8})$$

Using the product rule for derivatives and the incompressibility condition, the above equations can be rewritten as

$$0 = -\partial_r \overline{u'u'} - \frac{\overline{u'u'}}{r} + \frac{\bar{v}^2}{r} + \frac{\overline{v'v'}}{r} - \partial_r \bar{p} + \frac{1-\beta}{Re} \left(\partial_r \overline{T_{rr}} + \frac{\overline{T_{rr}} - \overline{T_{\theta\theta}}}{r} \right), \quad (\text{A9})$$

$$0 = -\partial_r \overline{u'v'} - \frac{2\overline{u'v'}}{r} + \frac{\beta}{Re} \left(\frac{1}{r} \partial_r (r \partial_r \bar{v}) - \frac{\bar{v}}{r^2} \right) + \frac{1-\beta}{Re} \left(\partial_r \overline{T_{r\theta}} + \frac{2\overline{T_{r\theta}}}{r} \right), \quad (\text{A10})$$

$$0 = -\partial_r \overline{u'w'} - \frac{\overline{u'w'}}{r} + \frac{1-\beta}{Re} \left(\partial_r \overline{T_{rz}} + \frac{\overline{T_{rz}}}{r} \right), \quad (\text{A11})$$

which is the final form of the axially averaged momentum equations.

We now multiply equations (A1)–(A3) by the velocity field and average over the axial direction to obtain an equation for the total kinetic energy. The resulting equation is

$$\begin{aligned} 0 = & -\overline{u\partial_r uu} - \overline{w\partial_z uu} - \overline{u\partial_r vv} - \overline{w\partial_z vv} - \overline{u\partial_r ww} - \overline{w\partial_z ww} - \overline{\partial_r pu} - \overline{\partial_z pw} \\ & + \frac{\beta}{Re} \left(\overline{u\nabla^2 u} - \frac{\overline{u^2}}{r^2} + \overline{v\nabla^2 v} - \frac{\overline{v^2}}{r^2} + \overline{w\nabla^2 w} \right) + \frac{1-\beta}{Re} \left(\overline{u\partial_r T_{rr}} + u \frac{(\overline{T_{rr}} - \overline{T_{\theta\theta}})}{r} \right. \\ & \left. + \overline{u\partial_z T_{rz}} + \overline{v\partial_r T_{r\theta}} + v \frac{2\overline{T_{r\theta}}}{r} + \overline{v\partial_z T_{\theta z}} + \overline{w\partial_r T_{rz}} + w \frac{\overline{T_{rz}}}{r} + \overline{w\partial_z T_{zz}} \right). \quad (\text{A12}) \end{aligned}$$

Introducing the decomposition in (A5) and subtracting equation (A10) multiplied by \bar{v} (i.e. the equation for the axially averaged kinetic energy), an equation for the kinetic energy of

the vortices is obtained

$$\begin{aligned}
 0 = & -\overline{u'\partial_r u'u'} - \overline{w'\partial_z u'u'} - \overline{u'\partial_r \bar{v}v'} - \overline{u'\partial_r v'\bar{v}} - \overline{u'\partial_r v'v'} - \overline{w'\partial_z v'\bar{v}} - \overline{w'\partial_z v'v'} \\
 & - \overline{u'\partial_r w'w'} - \overline{w'\partial_z w'w'} - \overline{\partial_r p'u'} - \overline{\partial_z p'w'} + \overline{\bar{v}\partial_r u'v'} + \frac{2\bar{v}u'v'}{r} \\
 & + \frac{\beta}{Re} \left(\overline{u'\nabla^2 u'} - \frac{\overline{u'^2}}{r^2} + \overline{v'\nabla^2 v'} - \frac{\overline{v'^2}}{r^2} + \overline{w'\nabla^2 w'} \right) \\
 & + \frac{1-\beta}{Re} \left(\overline{u'\partial_r T'_{rr}} + u' \frac{\overline{(T'_{rr} - T'_{\theta\theta})}}{r} + \overline{u'\partial_z T'_{rz}} + \overline{v'\partial_r T'_{r\theta}} + \frac{2v'T'_{r\theta}}{r} \right. \\
 & \left. + \overline{v'\partial_z T'_{\theta z}} + \overline{w'\partial_r T'_{rz}} + w' \frac{\overline{T'_{rz}}}{r} + \overline{w'\partial_z T'_{zz}} \right). \tag{A13}
 \end{aligned}$$

With some manipulation (using again the product rule for derivatives and the incompressibility condition), the above equation can be rewritten in the form

$$\begin{aligned}
 0 = & -\frac{1}{r} \partial_r \left[r \left(\frac{1}{2} (\overline{u'u'u'} + \overline{u'v'v'} + \overline{u'w'w'}) + \overline{p'u'} - \frac{\beta}{2Re} \partial_r (\overline{u'u'} + \overline{v'v'} + \overline{w'w'}) \right) \right. \\
 & \left. - \frac{1-\beta}{Re} (\overline{u'\partial_r T'_{rr}} + \overline{v'\partial_r T'_{r\theta}} + \overline{w'\partial_r T'_{rz}}) \right] - \overline{u'v'} \left(\partial_r \bar{v} - \frac{\bar{v}}{r} \right) \\
 & - \frac{\beta}{Re} \left(\overline{\partial_r u' \partial_r u'} + \overline{\partial_z u' \partial_z u'} + \overline{\partial_r v' \partial_r v'} + \overline{\partial_z v' \partial_z v'} + \overline{\partial_r w' \partial_r w'} + \overline{\partial_z w' \partial_z w'} + \frac{\overline{u'^2}}{r^2} + \frac{\overline{v'^2}}{r^2} \right) \\
 & - \frac{1-\beta}{Re} \left(\overline{\partial_r u' T'_{rr}} + \frac{\overline{(u' T'_{\theta\theta})}}{r} + \overline{\partial_z u' T'_{rz}} + \overline{\partial_r v' T'_{r\theta}} + \frac{\overline{v' T'_{r\theta}}}{r} + \overline{\partial_z v' T'_{\theta z}} + \overline{\partial_r w' T'_{rz}} \right. \\
 & \left. + \overline{\partial_z w' T'_{zz}} \right). \tag{A14}
 \end{aligned}$$

Finally, to obtain the volume average kinetic energy of the vortices that is presented in figure 6, (A14) is integrated over the radial direction. In doing so, the first term of the equation (i.e. the radial derivative of the quantity between brackets), which represents energy transport due to the various transport mechanisms at play, becomes zero and the integral kinetic energy equation reads as

$$\begin{aligned}
 0 = & - \int_0^1 \left(\overline{u'v'} \left(\partial_r \bar{v} - \frac{\bar{v}}{r} \right) \right) r \, dr - \frac{\beta}{Re} \int_0^1 \left(\overline{\partial_r u' \partial_r u'} + \overline{\partial_z u' \partial_z u'} + \overline{\partial_r v' \partial_r v'} + \overline{\partial_z v' \partial_z v'} \right. \\
 & \left. + \overline{\partial_r w' \partial_r w'} + \overline{\partial_z w' \partial_z w'} + \frac{\overline{u'^2}}{r^2} + \frac{\overline{v'^2}}{r^2} \right) r \, dr - \frac{1-\beta}{Re} \int_0^1 \left(\overline{\partial_r u' T'_{rr}} + \frac{\overline{(u' T'_{\theta\theta})}}{r} \right. \\
 & \left. + \overline{\partial_z u' T'_{rz}} + \overline{\partial_r v' T'_{r\theta}} + \frac{\overline{v' T'_{r\theta}}}{r} + \overline{\partial_z v' T'_{\theta z}} + \overline{\partial_r w' T'_{rz}} + \overline{\partial_z w' T'_{zz}} \right) r \, dr. \tag{A15}
 \end{aligned}$$

The equation above is the same as (3.1) but written in terms of its non-zero components. The first integral corresponds to the production of kinetic energy due to deviations of the velocity field from the axially averaged velocity (\mathcal{P}), the second integral is the viscous

dissipation of the kinetic energy (ϵ) and the third integral represents the contribution of the polymers (Π_e), which may be a production or a dissipation term depending on the fluid's elasticity.

Appendix B. The angular velocity current for steady axisymmetric vortex flow

Equation (3.5), used to decompose the radial flux of the angular velocity ω as a function of the contributions of the diffusive, convective and elastic transport mechanisms, was originally derived by Eckhardt *et al.* (2007) for fully turbulent Newtonian TCF and later extended to the viscoelastic case by Song *et al.* (2019). In this section, it is shown that the same equation can also be derived for the case of steady axisymmetric vortex flow. Following a procedure analogous to that in Eckhardt *et al.* (2007), the azimuthal momentum equation (A2) is averaged over the axial direction and one obtains

$$0 = -\overline{u\partial_r v} - \overline{w\partial_z v} - \frac{\overline{uv}}{r} + \frac{1}{Re} \left(\frac{1}{r} \partial_r (r \partial_r \bar{v}) - \frac{\bar{v}}{r^2} \right) + \frac{1-\beta}{Re} \left(\partial_r \overline{T_{r\theta}} + \frac{2\overline{T_{r\theta}}}{r} \right). \quad (\text{B1})$$

Using integration by parts, $\overline{w\partial_z v} = -\overline{v\partial_z w}$, and the continuity equation, $\partial_z w = -\partial_r u - u/r$, (B1) can be written as

$$0 = -\overline{u\partial_r v} - \overline{v\partial_r u} - \frac{2\overline{uv}}{r} + \frac{1}{Re} \left(\frac{1}{r} \partial_r (r \partial_r \bar{v}) - \frac{\bar{v}}{r^2} \right) + \frac{1-\beta}{Re} \left(\partial_r \overline{T_{r\theta}} + \frac{2\overline{T_{r\theta}}}{r} \right), \quad (\text{B2})$$

which can be rearranged into the form

$$0 = -r^{-2} \partial_r (r^2 \overline{uv}) + r^{-2} \left[\frac{1}{Re} \partial_r \left(r^3 \partial_r \frac{\bar{v}}{r} \right) \right] + r^{-2} \left[\frac{1-\beta}{Re} \partial_r (r^2 \overline{T_{r\theta}}) \right]. \quad (\text{B3})$$

If we now multiply by r^2 and introduce the angular velocity $\omega = v/r$ the equation becomes

$$0 = \partial_r \left(r^3 \left[\overline{u\omega} - \frac{1}{Re} \partial_r \bar{\omega} - \frac{1-\beta}{Re} \partial_r \frac{\overline{T_{r\theta}}}{r} \right] \right). \quad (\text{B4})$$

The equation above implies that the quantity

$$J^\omega = r^3 \left[\overline{u\omega} - \frac{1}{Re} \partial_r \bar{\omega} - \frac{1-\beta}{Re} \partial_r \frac{\overline{T_{r\theta}}}{r} \right], \quad (\text{B5})$$

does not change in the radial direction. Hence, it can be interpreted as a conserved current of the angular velocity across the annular gap. The three terms that appear in this equation correspond to the contributions of the different transport mechanisms (from left to right: transport due to convection, molecular diffusion and elastic stresses). Note that (B5) is essentially the same as that derived for fully turbulent flow (Song *et al.* 2019), with the only difference that while the average here is done only in space, time averaging is also needed in the turbulent case.

Appendix C. Additional results about the variation of the angular momentum fluxes with El

The variation of the angular velocity current, J^ω , with increasing El obtained in all simulations where the VMS regime is found is analogous to that exemplified in the figure 21 for the simulation presented in the § 3.1. Panels (a) and (b) of figure 22 show

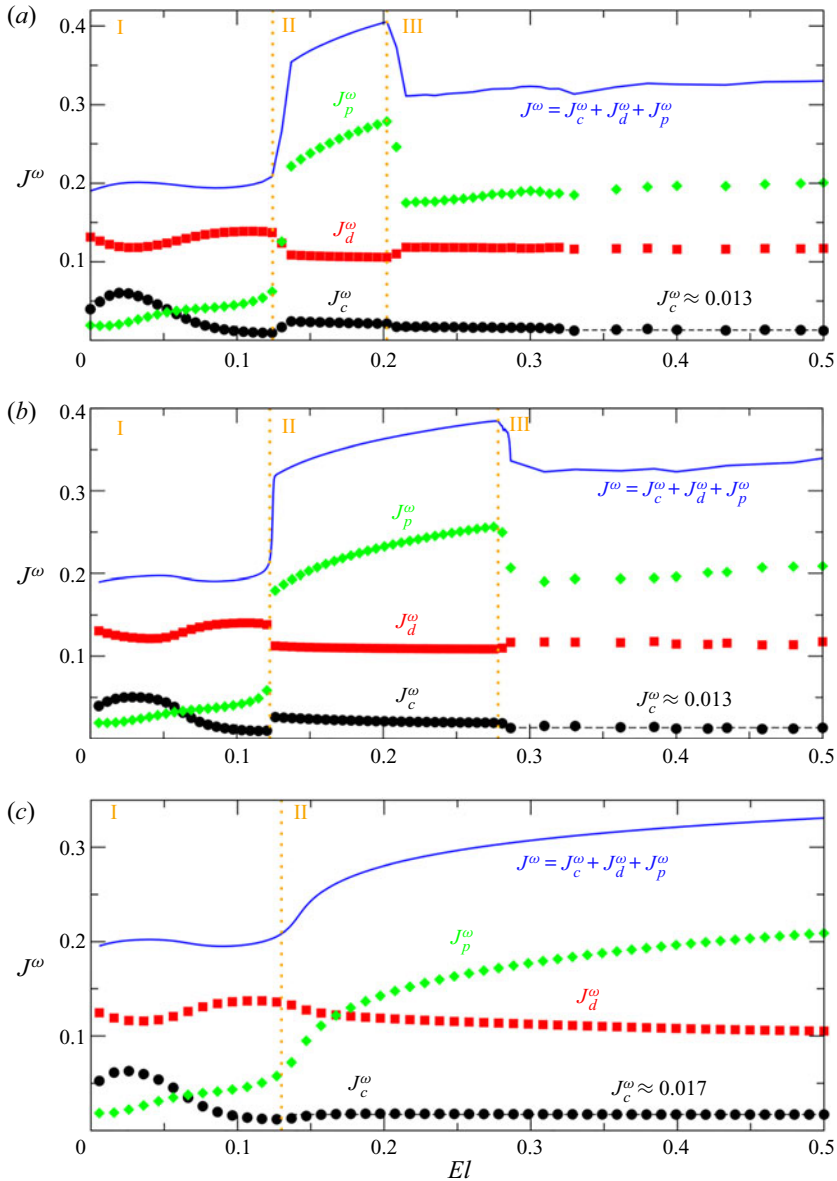


Figure 22. Variation of the angular velocity current, J^ω , and its components, J_c^ω , J_d^ω and J_p^ω , with El . Panels (a) and (b) correspond to simulations where the VMS regime takes place, whereas panel (c) exemplifies a case where this regime does not occur. More specifically, the data shown in panels (a) and (b) correspond to the simulations whose space–time diagrams are illustrated in figure 15(b) and (c), whereas the data shown in panel (c) corresponds to the simulation illustrated in figure 18(a).

the variation of J^ω and its components (J_c^ω , J_d^ω and J_p^ω) with El for the simulations illustrated in figure 15(b,c). These panels show clearly the existence of the three regimes described throughout the paper: the regime dominated by centrifugal effects (region I), the regime dominated by elastic effects where the flow pattern is steady (region II) and the regime characterized by spatio-temporal dynamics, including the VMS events (region III). The appearance of the latter regime is always accompanied by a slight

decrease in the convective contribution, J_c^ω (the contribution of the vortices), which subsequently oscillates around a mean value indicated by a (black) dashed line in the figures. It is important to note that such mean value is nearly the same in all cases, $J_c^\omega \approx 0.013$, suggesting that, at the Reynolds number at which the simulations are performed, $Re = 95$, this may be the critical level for which the DW fully decouple. For comparison, figure 22(c) shows the variation of J^ω with El in a simulation where the VMS regime does not occur. More specifically, it corresponds to the simulation where $L = 70$, whose space–time diagram is depicted in figure 18(a). In this simulation, after the elastic instability sets in (zone II), the convective and diffusive contributions, J_c^ω and J_d^ω , remain constant with increasing El , but the value at which of J_c^ω levels off ($J_c^\omega \approx 0.017$) is above that corresponding to the VMS regime. This observation is consistent with the hypothesis that DW get fully decoupled only when their contribution to the angular momentum transport reaches a critical level.

REFERENCES

- AL-MUBAIYEDH, U.A., SURESHKUMAR, R. & KHOMAMI, B. 1999 Influence of energetics on the stability of viscoelastic Taylor–Couette flow. *Phys. Fluids* **11** (11), 3217–3226.
- ANDERECK, C.D., LIU, S.S. & SWINNEY, H.L. 1986 Flow regimes in a circular Couette system with independently rotating cylinders. *J. Fluid Mech.* **164**, 155–183.
- AREF, H. 1983 Integrable, chaotic, and turbulent vortex motion in two-dimensional flows. *Annu. Rev. Fluid Mech.* **15** (1), 345–389.
- AVILA, M., GRIMES, M., LOPEZ, J.M. & MARQUES, F. 2008 Global endwall effects on centrifugally stable flows. *Phys. Fluids* **20** (10), 104104.
- BACHELOR, G.K. 2000 *An Introduction to Fluid Dynamics*. Cambridge University Press.
- BAUMERT, B.M. & MULLER, S.J. 1995 Flow visualization of the elastic Taylor–Couette instability in Boger fluids. *Rheol. Acta* **34** (2), 147–159.
- BAUMERT, B.M. & MULLER, S.J. 1997 Flow regimes in model viscoelastic fluids in a circular Couette system with independently rotating cylinders. *Phys. Fluids* **9** (3), 566–586.
- BAUMERT, B.M. & MULLER, S.J. 1999 Axisymmetric and non-axisymmetric elastic and inertio-elastic instabilities in Taylor–Couette flow. *J. Non-Newtonian Fluid Mech.* **83** (1), 33–69.
- BERIS, A.N. & DIMITROPOULOS, C.D. 1999 Pseudospectral simulation of turbulent viscoelastic channel flow. *Comput. Meth. Appl. Mech. Engng* **180** (3), 365–392.
- BIRD, R., DOTSON, P. & JOHNSON, N. 1980 Polymer solution rheology based on a finitely extensible bead–spring chain model. *J. Non-Newtonian Fluid Mech.* **7** (2), 213–235.
- CAGNEY, N., LACASSAGNE, T. & BALABANI, S. 2020 Taylor–Couette flow of polymer solutions with shear-thinning and viscoelastic rheology. *J. Fluid Mech.* **905**, A28.
- COLES, D. 1965 Transition in circular Couette flow. *J. Fluid Mech.* **21** (3), 385–425.
- CRUMEYROLLE, O., MUTABAZI, I. & GRISEL, M. 2002 Experimental study of inertioelastic Couette–Taylor instability modes in dilute and semidilute polymer solutions. *Phys. Fluids* **14** (5), 1681–1688.
- CZARNY, O., SERRE, E., BONToux, P. & LUEPTOW, R.M. 2003 Interaction between Ekman pumping and the centrifugal instability in Taylor–Couette flow. *Phys. Fluids* **15** (2), 467–477.
- DALLAS, V., VASSILICOS, J.C. & HEWITT, G.F. 2010 Strong polymer-turbulence interactions in viscoelastic turbulent channel flow. *Phys. Rev. E* **82** (6), 066303.
- DESSUP, T., TUCKERMAN, L.S., WESFREID, J.E., BARKLEY, D. & WILLIS, A.P. 2018 Self-sustaining process in Taylor–Couette flow. *Phys. Rev. Fluids* **3**, 123902.
- DUBIEF, Y., TERRAPON, V.E. & SORIA, J. 2013 On the mechanism of elasto-inertial turbulence. *Phys. Fluids* **25** (11), 110817.
- ECKHARDT, B., GROSSMANN, S. & LOHSE, D. 2007 Torque scaling in turbulent Taylor–Couette flow between independently rotating cylinders. *J. Fluid Mech.* **581**, 221–250.
- FENSTERMACHER, P.R., SWINNEY, H.L. & GOLLUB, J.P. 1979 Dynamical instabilities and the transition to chaotic Taylor vortex flow. *J. Fluid Mech.* **94** (1), 103–128.
- FOUXON, A. & LEBEDEV, V. 2003 Spectra of turbulence in dilute polymer solutions. *Phys. Fluids* **15** (7), 2060–2072.
- GORMAN, M. & SWINNEY, H.L. 1982 Spatial and temporal characteristics of modulated waves in the circular Couette system. *J. Fluid Mech.* **117**, 123–142.

- GROISMAN, A. & STEINBERG, V. 1996 Couette–Taylor flow in a dilute polymer solution. *Phys. Rev. Lett.* **77**, 1480–1483.
- GROISMAN, A. & STEINBERG, V. 1997 Solitary vortex pairs in viscoelastic Couette flow. *Phys. Rev. Lett.* **78**, 1460–1463.
- GROISMAN, A. & STEINBERG, V. 1998 Mechanism of elastic instability in Couette flow of polymer solutions: experiment. *Phys. Fluids* **10** (10), 2451–2463.
- GROISMAN, A. & STEINBERG, V. 2000 Elastic turbulence in a polymer solution flow. *Nature* **405**, 53–55.
- GROISMAN, A. & STEINBERG, V. 2004 Elastic turbulence in curvilinear flows of polymer solutions. *New J. Phys.* **6**, 29.
- HEGSETH, J.J., BAXTER, G.W. & ANDERECK, C.D. 1996 Bifurcations from Taylor vortices between corotating concentric cylinders. *Phys. Rev. E* **53**, 507–521.
- JONES, C.A. 1981 Nonlinear Taylor vortices and their stability. *J. Fluid Mech.* **102**, 249–261.
- JONES, C.A. 1985 The transition to wavy Taylor vortices. *J. Fluid Mech.* **157**, 135–162.
- KING, G.P., LEE, Y., LI, W., SWINNEY, H.L. & MARCUS, P.S. 1984 Wave speeds in wavy Taylor-vortex flow. *J. Fluid Mech.* **141**, 365–390.
- LACASSAGNE, T., CAGNEY, N. & BALABANI, S. 2021 Shear-thinning mediation of elasto-inertial Taylor–Couette flow. *J. Fluid Mech.* **915**, A91.
- LACASSAGNE, T., CAGNEY, N., GILLISSEN, J.J.J. & BALABANI, S. 2020 Vortex merging and splitting: a route to elastoinertial turbulence in Taylor–Couette flow. *Phys. Rev. Fluids* **5**, 113303.
- LANGE, M. & ECKHARDT, B. 2001 Vortex pairs in viscoelastic Couette–Taylor flow. *Phys. Rev. E* **64**, 027301.
- LARSON, R.G., SHAQFEH, E.S.G. & MULLER, S.J. 1990 A purely elastic instability in Taylor–Couette flow. *J. Fluid Mech.* **218**, 573–600.
- LATRACHE, N., ABCHA, N., CRUMEYROLLE, O. & MUTABAZI, I. 2016 Defect-mediated turbulence in ribbons of viscoelastic Taylor–Couette flow. *Phys. Rev. E* **93**, 043126.
- LATRACHE, N., CRUMEYROLLE, O. & MUTABAZI, I. 2012 Transition to turbulence in a flow of a shear-thinning viscoelastic solution in a Taylor–Couette cell. *Phys. Rev. E* **86**, 056305.
- LATRACHE, N. & MUTABAZI, I. 2021 Transition to turbulence via flame patterns in viscoelastic Taylor–Couette flow. *Eur. Phys. J. E* **44** (5), 63.
- LIU, N. & KHOMAMI, B. 2013 Elastically induced turbulence in Taylor–Couette flow: direct numerical simulation and mechanistic insight. *J. Fluid Mech.* **737**, R4.
- LOPEZ, J.M. & AVILA, M. 2017 Boundary-layer turbulence in experiments on quasi-Keplerian flows. *J. Fluid Mech.* **817**, 21–34.
- LOPEZ, J.M., CHOUERI, G.H. & HOF, B. 2019 Dynamics of viscoelastic pipe flow at low Reynolds numbers in the maximum drag reduction limit. *J. Fluid Mech.* **874**, 699–719.
- LÓPEZ, J.M., FELDMANN, D., RAMPP, M., VELA-MARTÍN, A., SHI, L. & AVILA, M. 2020 nsCouette—a high-performance code for direct numerical simulations of turbulent Taylor–Couette flow. *SoftwareX* **11**, 100395.
- MARCUS, P.S. 1984a Simulation of Taylor–Couette flow. Part 1. Numerical methods and comparison with experiment. *J. Fluid Mech.* **146**, 45–64.
- MARCUS, P.S. 1984b Simulation of Taylor–Couette flow. Part 2. Numerical results for wavy-vortex flow with one travelling wave. *J. Fluid Mech.* **146**, 65–113.
- MARTINAND, D., SERRE, E. & LUEPTOW, R.M. 2014 Mechanisms for the transition to waviness for Taylor vortices. *Phys. Fluids* **26** (9), 094102.
- MULLER, S.J., LARSON, R.G. & SHAQFEH, E.S. 1989 A purely elastic transition in Taylor–Couette flow. *Rheol. Acta* **28** (6), 499–503.
- RUELLE, D. & TAKENS, F. 1971 On the nature of turbulence. *Commun. Math. Phys.* **20**, 167–192.
- SAMANTA, D., DUBIEF, Y., HOLZNER, M., SCHÄFER, C., MOROZOV, A.N., WAGNER, C. & HOF, B. 2013 Elasto-inertial turbulence. *Proc. Natl Acad. Sci.* **110** (26), 10557–10562.
- SHAQFEH, E.S.G. 1996 Purely elastic instabilities in viscometric flows. *Annu. Rev. Fluid Mech.* **28** (1), 129–185.
- SHI, L., RAMPP, M., HOF, B. & AVILA, M. 2015 A hybrid MPI-openmp parallel implementation for pseudospectral simulations with application to Taylor–Couette flow. *Comput. Fluids* **106**, 1–11.
- SONG, J., LIN, F., LIU, N., LU, X.-Y. & KHOMAMI, B. 2021a Direct numerical simulation of inertio-elastic turbulent Taylor–Couette flow. *J. Fluid Mech.* **926**, A37.
- SONG, J., TENG, H., LIU, N., DING, H., LU, X.-Y. & KHOMAMI, B. 2019 The correspondence between drag enhancement and vortical structures in turbulent Taylor–Couette flows with polymer additives: a study of curvature dependence. *J. Fluid Mech.* **881**, 602–616.
- SONG, J., WAN, Z.-H., LIU, N., LU, X.-Y. & KHOMAMI, B. 2021b A reverse transition route from inertial to elasticity-dominated turbulence in viscoelastic Taylor–Couette flow. *J. Fluid Mech.* **927**, A10.

Vortex merging and splitting events in viscoelastic TCF

- TAYLOR, G.I.S. 1923 Stability of a viscous liquid contained between two rotating cylinders. *Phil. Trans. R. Soc. A* **223**, 289–343.
- THOMAS, D.G., KHOMAMI, B. & SURESHKUMAR, R. 2009 Nonlinear dynamics of viscoelastic Taylor–Couette flow: effect of elasticity on pattern selection, molecular conformation and drag. *J. Fluid Mech.* **620**, 353–382.
- THOMAS, D.G., SURESHKUMAR, R. & KHOMAMI, B. 2006 Pattern formation in Taylor–Couette flow of dilute polymer solutions: dynamical simulations and mechanism. *Phys. Rev. Lett.* **97**, 054501.
- WERELEY, S.T. & LUEPTOW, R.M. 1998 Spatio-temporal character of non-wavy and wavy Taylor–Couette flow. *J. Fluid Mech.* **364**, 59–80.
- WILLIS, A.P. 2017 The openpipeflow Navier–Stokes solver. *SoftwareX* **6**, 124–127.
- XI, L. & GRAHAM, M.D. 2010 Turbulent drag reduction and multistage transitions in viscoelastic minimal flow units. *J. Fluid Mech.* **647**, 421–452.
- YAMANI, S., KESHAVERZ, B., RAJ, Y., ZAKI, T.A., MCKINLEY, G.H. & BISCHOFBERGER, I. 2021 Spectral universality of elastoinertial turbulence. *Phys. Rev. Lett.* **127**, 074501.
- ZHU, Y., SONG, J., LIN, F., LIU, N., LU, X. & KHOMAMI, B. 2022 Relaminarization of spanwise-rotating viscoelastic plane Couette flow via a transition sequence from a drag-reduced inertial to a drag-enhanced elasto-inertial turbulent flow. *J. Fluid Mech.* **931**, R7.
- ZHU, Y., SONG, J., LIU, N., LU, X. & KHOMAMI, B. 2020 Polymer-induced flow relaminarization and drag enhancement in spanwise-rotating plane Couette flow. *J. Fluid Mech.* **905**, A19.